

## Original Article

## Airport infrastructure risk to liquefaction by deploying multi-modal data and remote sensing

Maria Taftsoglou <sup>a</sup>, George Papathanassiou <sup>b</sup>, Sotirios Valkaniotis <sup>b</sup>, Sotirios Argyroudis <sup>c,e,\*</sup>, Stergios-Aristoteles Mitoulis <sup>d,e</sup>

<sup>a</sup> Department of Civil Engineering, Democritus University of Thrace, Xanthi, Greece

<sup>b</sup> Department of Geology, Aristotle University of Thessaloniki, Thessaloniki, Greece

<sup>c</sup> Department of Civil and Environmental Engineering, Brunel University of London, Uxbridge, UK

<sup>d</sup> The Bartlett School of Sustainable Construction, University College London, UK

<sup>e</sup> MetaInfrastructure.org, London, UK

## ARTICLE INFO

## Keywords:

Liquefaction risk assessment  
Airport infrastructure  
Geohazards  
Remote sensing  
Seismic vulnerability

## ABSTRACT

Airports are critical components of transport infrastructure, contributing to regional socioeconomic vitality and serving as key hubs for emergency response during natural disasters. However, their operations are highly vulnerable to geohazards such as earthquake-induced soil liquefaction and associated ground failures. Despite this vulnerability, there is currently a lack of rapid, regionally scalable tools for assessing liquefaction-related risks specific to airport infrastructure. This paper for the first time in the literature addresses this gap by introducing a practical, geomorphology-informed methodology for the preliminary identification of liquefaction-prone areas and the rapid assessment of risk to airport infrastructure. The proposed approach leverages multi-modal data, including surface geological mapping, tailored remote sensing inputs, and established seismic risk models, to develop liquefaction susceptibility maps and estimate potential damage. The methodology is applied to a real-world airport case study under a representative seismic scenario, revealing that large sections of the runway and taxiways are situated on highly susceptible soils. The HAZUS methodology is employed to assess potential losses and is validated using data from three international airports that have experienced documented liquefaction-related damage. This study provides a novel, scalable, and cost-effective framework that can be applied globally to support airport operators, risk engineers, and insurers in rapidly identifying vulnerable zones, prioritizing inspections, and developing targeted mitigation strategies. It contributes to advancing geotechnical risk assessment by bridging regional-scale mapping with infrastructure-specific vulnerability analysis. The methodology has the potential to be extended and applied to other critical infrastructure—such as ports, highways, railways, and industrial facilities—located in areas susceptible to liquefaction.

## Introduction

Transport infrastructure is increasingly vulnerable to a broad spectrum of geohazards and climate-related impacts, which threaten its functionality, safety, and long-term sustainability. In addition to well-documented seismic risks, infrastructures such as airports face growing exposure to hazards exacerbated by climate change, including ground instability, subsidence, and extreme weather events. The interaction between physical hazards and infrastructure performance must be understood through integrated, spatially aware risk assessment frameworks to inform adaptive planning and resilience strategies [1].

Among geohazards, earthquakes remain a significant threat, particularly when compounded by secondary effects such as soil liquefaction and landslides. Liquefaction refers to the loss of soil strength and stiffness due to increased pore water pressure during seismic shaking, causing saturated, loose granular soils to behave like a fluid [2]. This phenomenon is typically triggered in fluvial plains, coastal zones, and reclaimed lands with young, water-saturated sediments [3–8]. The resulting ground deformation—settlement, lateral spreading, and foundation failure—can inflict extensive damage on critical infrastructure systems, including airports.

As functionally critical and spatially constrained components of the transport network, airports are particularly susceptible to

\* Corresponding author.

E-mail address: [sotirios.argyroudis@brunel.ac.uk](mailto:sotirios.argyroudis@brunel.ac.uk) (S. Argyroudis).

## Nomenclature

### List of symbols

$K_M$	moment magnitude (M) correction factor
$K_W$	correction factor for groundwater depths ( $d_w$ ) other than 5ft (1.52 m)
$P_{ml}$	proportion of map unit susceptible to liquefaction
IM	Intensity Measure
M	moment magnitude
$P[\text{Liquefaction}_{sc}]$ or $PL_{sc}$	probability of liquefaction
$P(DS = ds   IM)$	Probability that the airport asset is in a specific damage state $ds$ , conditional on the imposed intensity measure (IM).
$P[\text{Liquefaction}_{sc}   \text{PGA} = a]$	conditional liquefaction probability for a given susceptibility category at a specified level of peak ground acceleration
$P_f(DS \geq ds   IM)$	Probability that the airport asset damage state $DS$ meets or exceeds a specified damage threshold $ds$ , conditional on the imposed intensity measure (IM). The damage states typically include: s/m (slight/minor), e (extensive), c (complete)
PGA	Peak Ground Acceleration
PGD	Permanent Ground Deformation
RR	Repair Ratio
$V_{S30}$	average shear-wave velocity in the upper 30 m of the ground
CTI	compound topographic index

geohazards—especially soil liquefaction—due to their frequent location in low-lying, reclaimed, or alluvial terrain. Runways, taxiways, and critical support systems (e.g. control towers, fuel pipelines, and communication infrastructure) require flat, open land, which often coincides with regions characterised by loose, saturated soils. These conditions, when combined with seismic activity, create a high risk for liquefaction-induced ground failure [9–11]. Beyond their operational sensitivity, the societal and economic importance of airports for tourism and trade, they are vital hubs for emergency response and humanitarian aid, enabling the rapid mobilisation of resources and evacuation of affected populations following natural (e.g. earthquakes) or human induced disasters (e.g. conflicts). According to the Airport Council International [12], European airports alone support 14 million jobs and contribute €851 billion to GDP—approximately 5 % of the continent’s total economic output. Given these critical functions, understanding and mitigating liquefaction risk in airport environments is essential.

Historical earthquake events have demonstrated the diverse and often severe impacts of liquefaction on airport infrastructure, ranging from pavement cracking and settlement to control tower and utility failures. For instance, during the 1989 Loma Prieta earthquake (USA), the main runway of Oakland International Airport experienced extensive liquefaction, including sand boils and lateral spreading [13–15], with repair costs estimated at \$5.7 million [16]. Similar effects were observed at Alameda Naval Air Station, forcing runway closures for up to three months [17]. The 1994 Northridge earthquake (USA) damaged the control tower at Van Nuys Airport [18], while the 1995  $M_w$  6.9 Kobe earthquake (Japan) caused surface cracks and structural impacts at Kansai and Itami Airports [19]. During the 2001 Nisqually earthquake (USA), King County International Airport experienced extensive ground deformation and pavement cracking, with total repair and upgrade costs reaching \$4.4 million [20]. Most recently, the 2023 Türkiye-Syria earthquakes triggered severe liquefaction-induced damage at Hatay International Airport, particularly affecting the eastern runway [21]. These examples underline the urgent need for proactive, regionally scalable methods to assess and mitigate airport vulnerability to

liquefaction.

Over recent decades, multiple methodologies have been developed to evaluate liquefaction potential and its impacts on infrastructure. Widely used approaches include the Liquefaction Potential Index (LPI) and Liquefaction Severity Number (LSN), which assess liquefaction risk based on in-situ test data such as the Standard Penetration Test (SPT) and Cone Penetration Test (CPT) [22–25]. Complementary tools such as HAZUS, SYNER-G, and REDARS 2 [26–29] provide standardised frameworks for assessing liquefaction risk for transportation systems. Nonetheless, accurate site-specific vulnerability assessments require detailed geotechnical testing, which can be costly and time-consuming. Laboratory analyses (e.g. grain size distribution, Atterberg limits) and in-situ methods are necessary to estimate safety factors and determine the liquefaction potential of each soil layer [30–32]. Moreover, they provide essential parameters for the development and calibration of numerical models (Finn, UBC Sand, PM4Sand, SANISAND etc.), allowing the simulation of the soil response during liquefaction [33–38] and consequently the estimation of the potential for vertical or lateral ground displacement and structural damage under various earthquake scenarios [39].

This renders such evaluations impractical for large-scale or time-sensitive applications. At the regional level, susceptibility assessment relies on geomorphological indicators such as sediment age, depositional environment, and groundwater depth. Established frameworks for regional-scale mapping include the methodologies of Youd and Perkins [40], Wakamatsu [41], CDMG [42], and Witter et al. [43]. However, these methods are often hindered by the limited availability or insufficient resolution of geomorphological data.

Remote sensing technologies address these limitations by providing multi-temporal observations of the surficial geological environment. Particularly, optical satellite imagery allows the identification of variations in soil color and moisture, facilitating the detection not only of areas affected by liquefaction phenomena but also of the different geomorphological features, in which such occurrences are observed. In addition, radar-based remote sensing techniques, such as InSAR and LiDAR, have proven very useful in monitoring post-seismic ground deformation over large areas [44,45]. For instance, employing a combination of very high-resolution optical satellite imagery and InSAR coherence analysis, Taftsgolou et al. [21] identified liquefaction phenomena in the eastern runway of Hatay International airport after the 2023 Türkiye-Syria earthquakes.

Despite their global economic significance—with an estimated total impact of \$4.1 trillion (Air Transport Action Group – ATAG)—airports remain particularly vulnerable to seismic ground deformations, especially liquefaction. Given their dual role in economic connectivity and emergency response, ensuring their resilience is vital. This study introduces a novel, scalable, and data-efficient methodology for assessing liquefaction-related risk to airport infrastructure at a regional scale, addressing the need for rapid, transferable tools in seismic risk management.

The proposed approach integrates remote sensing, geomorphological mapping, and scenario-based seismic modelling to generate susceptibility classifications, estimate liquefaction probability, compute permanent ground deformation (PGD), and evaluate potential economic losses—all without requiring detailed site-specific investigations. The methodology is demonstrated using Kavala International Airport (KVA) in North Greece as a representative case study. The method is further validated using historical case studies from three international airports affected by liquefaction. By bridging regional geomorphic classification with infrastructure-specific risk estimation, this research offers a generalisable framework to support airport operators, risk engineers, and policymakers in identifying vulnerable assets and developing targeted mitigation strategies [46,47].

## Methodology

The proposed methodology is structured into two main phases comprising a total of nine steps. **Phase I** follows a workflow adapted from Taftsgolou et al. [48] and focuses on assessing the liquefaction

susceptibility of the study area through the following three steps: (1) data collection and processing, (2) mapping geomorphological features, (3) classification of susceptible geological units, and liquefaction susceptibility mapping. **Phase II** is dedicated to evaluating the risk to critical infrastructure within the same region. It comprises an additional

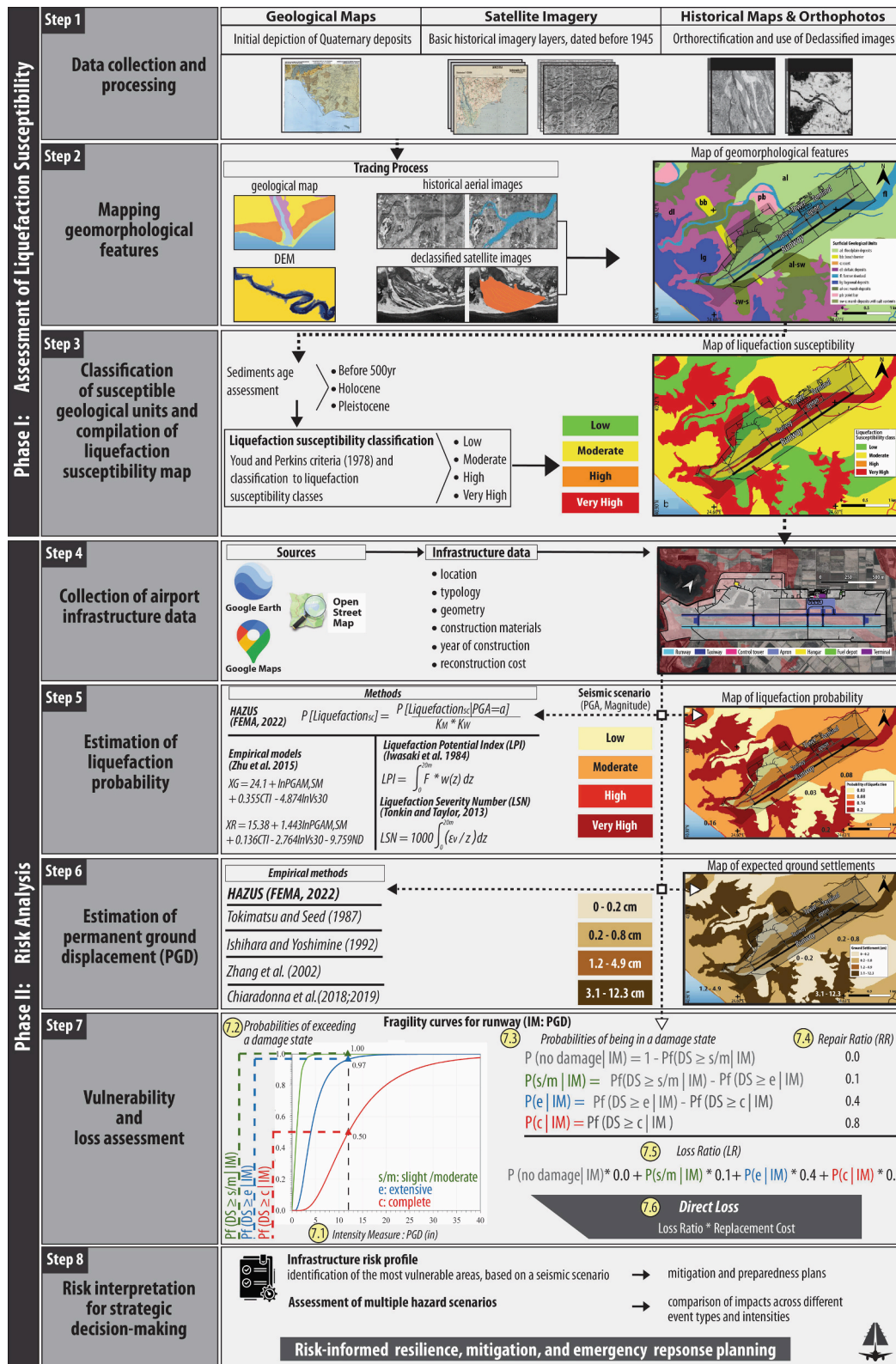


**Fig. 1.** Methodology for assessing liquefaction risk for airport infrastructure by deploying multi-modal data and remote sensing.

five steps: (4) collection of airport infrastructure data, (5) estimation of liquefaction probability, (6) estimation of permanent ground displacement (PGD), (8) vulnerability and loss assessment, and (9) risk assessment. The overall workflow is illustrated in Fig. 1.

#### Phase I: Assessment of liquefaction susceptibility

**Step 1 – Data collection and processing.** This phase begins with the acquisition and preparation of geospatial datasets at a regional scale (see Step 1 in Fig. 1). The resolution and quality of the resulting susceptibility map depend heavily on the availability and accuracy of geological and topographic data. To address potential data limitations, a combination of remote sensing sources and historical cartographic datasets is utilised, including:

- **Geological map sheets:** Serve as the primary data source for delineating Quaternary deposits, such as fluvial, floodplain and lagoonal. Nevertheless, due to their limited information concerning the geomorphological evolution of the deposits, remote sensing data are employed.
- **Historical aerial imagery:** Provides valuable insights into pre-modern surficial geomorphology. Imagery predating the 1950 s is preferred to minimise distortions from anthropogenic alterations, though availability varies by location and is typically obtained from national or regional mapping authorities. Acquisition relies on image overlap, where common points identified in successive pairs are used for mosaicking and generating orthophoto maps of the study area.
- **High-resolution (<5 m) digital elevation models (DEMs):** Derived from stereo aerial or satellite imagery or from airborne LiDAR surveys. These are instrumental in detecting subtle geomorphic features such as river levees and free-face areas prone to lateral spreading. Availability of LiDAR topographic surveys is limited but can be substituted by extracting a high-resolution digital surface model (DSM) from stereo very high resolution (VHR) optical satellite imagery such as WorldView, SPOT6/7 or Pleiades.
- **Declassified satellite imagery (e.g., Corona, Hexagon):** Grayscale imagery from the 1960 s–1970 s that provides broader coverage than traditional aerial photographs. These datasets significantly reduce processing time by capturing larger areas, but they require orthorectification before analysis. Since images are taken at oblique angles and are subject to terrain-induced distortions, software such as ERDAS IMAGINE is typically used to project them onto a horizontal plane, enabling accurate georeferencing.
- **Contemporary VHR satellite imagery and aerial orthophotos:** Although recent surface modifications may obscure some landforms, relict geomorphological features can often still be identified through variations in colour, wavelength signatures, and surface texture. Imagery acquired during periods of low vegetation cover or high surface moisture is particularly effective for this purpose. Such datasets are widely accessible through digital archives (e.g., Copernicus Data Library, ESA) or other repositories (e.g., SPOT World Heritage, ALOS AVNIR).

Following collection, these layers are imported into a GIS environment and analysed individually in relation to the geological and geomorphological formations they represent. The integration of these datasets enables the reconstruction of the area's geomorphological evolution and supports the production of a surficial geology map.

**Step 2 – Mapping geomorphological features.** In this step, geomorphological features are traced using multi-temporal and historical imagery. This enables identification of surficial units such as active and abandoned river channels, point bars, beach ridges, and coastal dunes—even in areas where these have been obscured by land development or the rapid evolution of the fluvial system, e.g. due to climate or human activity.

Specifically, beginning with the geologic map of the study area, the

boundaries of the Quaternary sediments are delineated (Step 2.1 in Fig. 2). These include fluvial, floodplain, and marsh deposits; Pleistocene deposits; as well as water bodies such as lagoons and the main river channel. Elevation transitions represented in the DEM (Step 2.2 in Fig. 2) provide an accurate depiction of the boundaries between colluvial and floodplain sediments and also enable the identification of paleochannels and levees (both natural and anthropogenic) associated with the river course.

Historical aerial imagery (Step 2.3 in Fig. 2) allows recognition of elements of the hydrographic network, such as abandoned channels and point bars. Point bars typically accumulate along the inner sides of meander bends and often display characteristic banding reflecting successive stages of growth. Dune deposits mapped along the coastal front show striations, while elongate sand ridges parallel to the shoreline represent beach-barrier formations. In a deltaic setting, aerial imagery assists in distinguishing deltaic deposits—appearing as brighter zones near river mouths—from lagoonal deposits, which are darker, as are marsh deposits situated within the floodplain interior.

Declassified satellite imagery (Step 2.4 in Fig. 2) captures intermediate changes in surficial geology during the geomorphic evolution of the area. These datasets enable mapping of hydrographic changes such as channel desiccation, as well as progradation and erosion affecting deltaic and coastal deposits.

Finally, high- and very high-resolution satellite imagery (Step 2.5 in Fig. 2) supports monitoring of modern landscape alterations, including infrastructure projects (e.g., transportation corridors, dams, airports). Their multispectral properties also facilitate the detection of relict geomorphic features, especially under low vegetation cover or high surface moisture.

**Step 3 – Classification of susceptible geological units and compilation of liquefaction susceptibility map.** Geological and geomorphological maps are used to classify surficial units according to age (<500 years, Holocene, Pleistocene) and depositional environment. The assessment also considers relative surface modification, topographic position, and expert judgement. Liquefaction susceptibility is then determined following the criteria of Youd and Perkins [40], which categorise the area into four classes: low, moderate, high, and very high susceptibility (see Step 3 in Fig. 1).

#### Phase II: Risk analysis

**Step 4 – Collection of airport infrastructure data.** Before initiating the risk analysis, detailed information on the airport infrastructure is collected to support the subsequent vulnerability and loss assessment. This includes data on the location, typology, geometry, construction materials, year of construction, and estimated reconstruction costs for key assets such as runways, taxiways, aprons, terminal buildings, and control towers. Data sources include Google Earth, OpenStreetMap, and any available documentation such as procurement records, design specifications, structural drawings and maintenance reports. This data is organised into GIS layers, which allows for direct spatial integration with the liquefaction susceptibility map developed in Step 3. This geospatial alignment facilitates overlay analyses, ensuring that critical infrastructure elements can be accurately linked to their underlying geotechnical context. It also enables targeted estimation of PGD in Step 6, focusing specifically on the areas where airport facilities are located.

**Step 5 – Estimation of liquefaction probability.** With the susceptibility map from Phase I in place, this step estimates the probability of liquefaction under a defined seismic scenario. Several methods are available for this purpose:

- **Liquefaction Potential Index (LPI) and Liquefaction Severity Number (LSN) [22,49,50]:** Having been applied in many studies [23–25,51] these indices integrate factors of safety for individual soil layers (up to 20 m depth) and are calculated based on in-situ test data such as SPT and CPT [30–32,52,53].

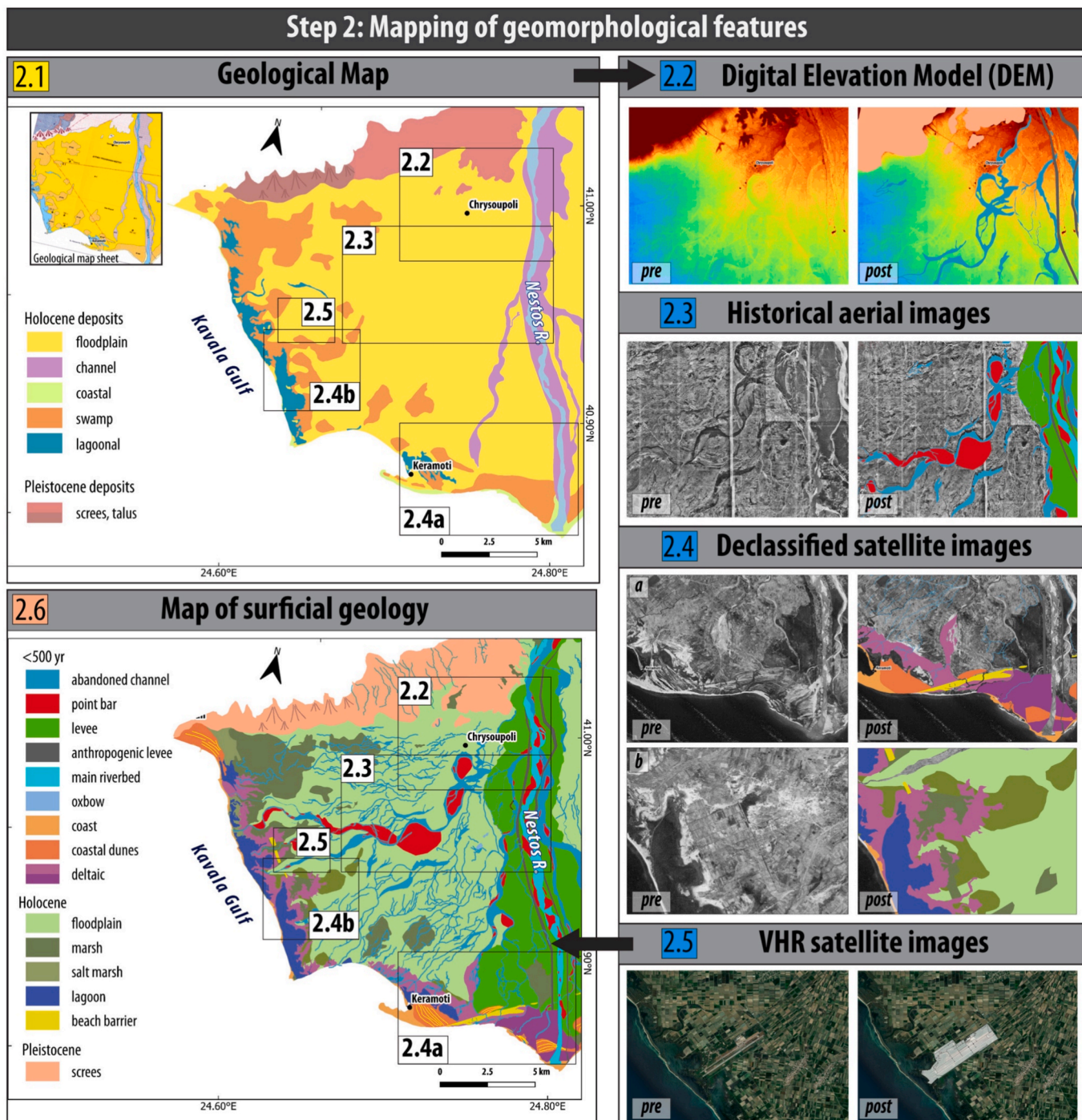


**Fig. 2.** Mapping of geomorphological features, using (2.1) geological maps, (2.2) Digital Elevation Model (DEM), (2.3) historical aerial imagery, (2.4) declassified satellite data and (2.5) very high resolution (VHR) satellite imagery, followed by the compilation of a surficial geology map (2.6). The maps illustrate the western Nestos delta in northern Greece (modified after [48]). “Pre” and “Post” labels denote data before and after geomorphological feature mapping, respectively.

- **Empirical models by Zhu et al. [54]:** Utilise predictors such as the compound topographic index (CTI), the average shear-wave velocity in the upper 30 m of the ground ( $V_{S30}$ ), magnitude-scaled Peak Ground Acceleration ( $PGA_M$ ) and PGA derived directly from Shake-Maps ( $PGA_{SM}$ ), surface moisture (SM), magnitude weighting factor (MWF), and distance from the coast (ND). These models offer both global (XG) and region-specific (XR) (coastal sedimentary basins) linear formulations for estimating liquefaction likelihood to assess the liquefaction likelihood.
- **Federal Emergency Managements Agency guidelines [29]:** provide a simplified method, in which the likelihood of experiencing liquefaction at a specific location is primarily influenced by soil susceptibility, ground shaking amplitude and duration, and groundwater depth.

Given the study's objective for regional-scale rapid assessment, the HAZUS framework is adopted due to its efficiency and simplified data requirements. The probability of liquefaction is estimated using equation (1):

$$P[\text{Liquefaction}_{sc}] = \frac{P[\text{Liquefaction}_{sc} | \text{PGA} = a]}{K_M * K_W} * P_{ml} \quad (1)$$

where:

- $P[\text{Liquefaction}_{sc} | \text{PGA} = a]$ : is the conditional liquefaction probability for a given susceptibility category at a specified level of peak ground acceleration (PGA)
- $K_M = 0.0027M^3 - 0.0267M^2 - 0.2055M + 2.9188$ : is the moment magnitude (M) correction factor
- $K_W = 0.022d_w + 0.93$ : is the correction factor for groundwater depths ( $d_w$ ) other than 5ft (1.52 m)
- $P_{ml}$ : proportion of map unit susceptible to liquefaction

Considering that for a given subsoil category, liquefaction is unlikely to occur over the whole portion of the geologic map,  $P_{ml}$  parameter is used to assess the probability of liquefaction at any given location. As the non-susceptible portions are expected to be smaller for higher susceptibilities,  $P_{ml}$  is inserted in order to quantify the proportion of geologic map unit deemed susceptible to liquefaction, i.e., the likelihood of susceptible conditions existing at any given location within the unit. Table 1 presents the default  $P_{ml}$  values based on regional studies.

**Step 6 – Estimation of permanent ground displacement (PGD).** To support the preliminary assessment of infrastructure damage, this step estimates liquefaction-induced ground settlement. Relationships from Tokimatsu and Seed [55], Ishihara and Yoshimine [56], and Zhang et al. [57] can be used to correlate volumetric strain with relative density and factor of safety for clean sands. Moreover, laboratory cyclic shear tests on sands specimen, can demonstrate how combined shear and principal stress rotation contribute to settlement [58]. Although recent studies (e.g., [59,60]) recommend non-linear effective stress analyses in 1-D conditions for greater accuracy, such methods are data-intensive and less practical for regional-scale applications. Therefore, HAZUS approach is adopted here to estimate PGD, by multiplying the probability of liquefaction (Step 5) by the representative settlement amplitude per susceptibility category (Table 2).

**Step 7 – Vulnerability and loss assessment.** Fragility functions are used to estimate damage probabilities for a given intensity measure, such as PGD [61,62]. Due to the limited availability of vulnerability models for airport infrastructure, the fragility functions from the HAZUS methodology are commonly adopted. These functions define the probabilities of exceeding specific damage states (slight, moderate, extensive, and complete) based on PGD values calculated in Step 6. To estimate expected losses, representative repair ratios—defined as the ratio of repair to replacement cost—are applied to each damage state. The average loss ratio is then calculated by weighting these repair ratios with the corresponding damage probabilities, allowing for the assessment of total expected loss under the selected seismic scenario.

**Step 8 – Risk interpretation for strategic decision-making.** The final step involves the integration of previous analytical outputs to generate a comprehensive risk profile for the airport under the selected seismic scenario. This profile supports the identification of the most vulnerable areas within the facility and informs prioritised decision-making for mitigation and preparedness planning. This step may also involve the assessment of multiple hazard scenarios, allowing stakeholders to compare impacts across different event types or intensities. By consolidating risk information into a unified framework, the process

**Table 1**  
Proportion of map unit susceptible to liquefaction.

Mapped Relative Susceptibility	Proportion of Map Unit ( $P_{ml}$ )
Very High	0.25
High	0.20
Moderate	0.10
Low	0.05

**Table 2**  
Ground settlement amplitudes for liquefaction susceptibility categories.

Relative susceptibility	Settlement (cm)
Very High	30.50
High	15.20
Moderate	5.08
Low	2.50
Very Low	0.00
None	0.00

facilitates evidence-based strategies for enhancing infrastructure resilience, emergency response planning, and long-term investment decisions.

### Case Study

Kavala International Airport (KVA) is situated on the western margin of the Nestos delta plain in Thrace, northern Greece. Constructed in the 1980s on recent Holocene deposits and located near active onshore and offshore fault systems, KVA is of particular interest for the analysis of liquefaction susceptibility and vulnerability of its units. This section demonstrates the implementation of the proposed methodology for assessing liquefaction susceptibility and associated risk, as outlined in the previous section.

#### Phase I – Liquefaction susceptibility assessment

In line with **Step 1**, geological map sheets at a scale of 1:50,000 (Hellenic Survey of Geology and Mineral Exploration – HSGME) were collected. Historical orthophoto maps dated prior to 1945 (Hellenic Cadastre) and declassified CORONA (KH-4) satellite imagery from 1960 and 1968 (USGS/NARA) were used to reconstruct the surficial landscape prior to extensive land modifications. These were complemented by VHR satellite imagery from Google Earth to assess current land cover conditions, and a digital surface model (DSM) with 5 m resolution (Hellenic Cadastre) to enhance the interpretation of subtle topographic features.

Initial review of the official geological maps, published by HSGME, indicated undivided alluvial and floodplain deposits across the area, with the airport itself situated on swamp and floodplain sediments of Holocene age. However, further interpretation using remote sensing, topographic data and historical imagery, as part of **Step 2**, enabled the delineation of geomorphological features previously obscured by anthropogenic alterations (Fig. 3). The analysis revealed that KVA was largely constructed on former fluvial and deltaic deposits associated with a historic river network that was diverted and entrenched in 1952. The traced features included abandoned channels, point bars, beach barriers, floodplain and deltaic deposits, as well as marsh sediments. The resulting geomorphological map indicated that a significant portion of airport facilities, including parts of the runway, lie on the footprint of an abandoned river branch of old estuaries, while the remaining infrastructure spans floodplain and marshland formations (Fig. 3, Fig. 4).

In **Step 3**, sediment units were classified based on age (younger than 500 years, Holocene, and Pleistocene), and depositional environment. Using the Youd and Perkins [40] criteria, the most susceptible units were identified as abandoned meanders, point bars, beach barriers, and deltaic deposits—primarily located in the central, northwestern, and southwestern parts of the airport. High susceptibility was also identified near the coastal zone. Floodplain deposits, which dominate the area, were classified as moderately susceptible, while marsh deposits along the northeastern and southeastern margins were assigned low susceptibility. Based on this classification, a liquefaction susceptibility map was developed, categorising the airport site into zones of low, moderate, high, and very high susceptibility (Fig. 4).

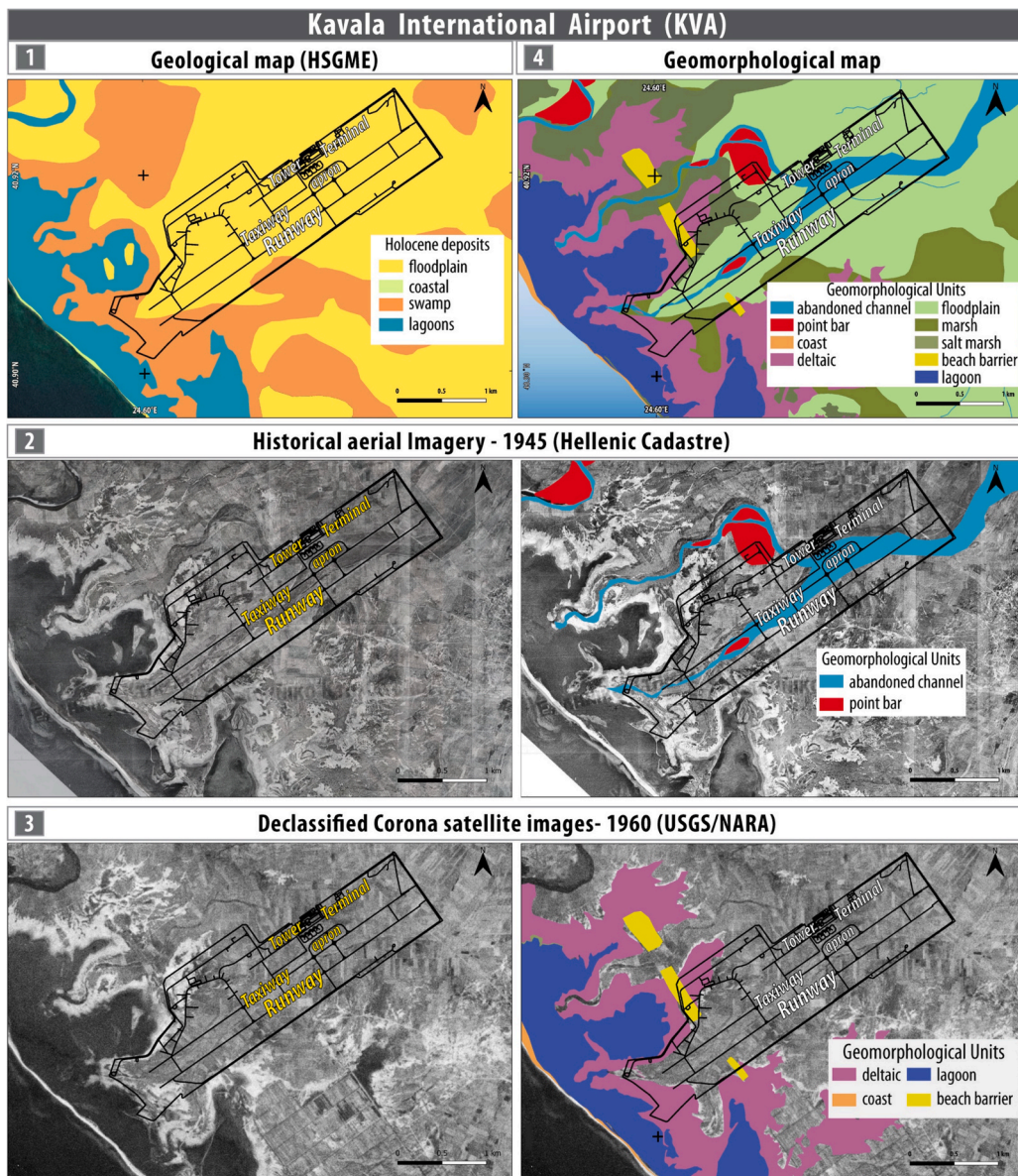


**Fig. 3.** Use of (1) geological map, (2) historical aerial images and (3) declassified satellite images for the compilation of the geomorphological map for KVA region (4).

#### Phase II – Risk Analysis

In accordance with **Step 4**, a GIS-based map of the KVA airport infrastructure was developed using data sourced primarily from Google Maps (Fig. 5). This map includes the location and spatial footprints of critical components such as runways, taxiways, aprons, and main buildings. The geospatial organisation of this information enabled direct overlay with the liquefaction susceptibility zones established in Step 3, ensuring spatial consistency across the analysis. For the purposes of the risk assessment, particular emphasis was placed on the runways, taxiways, and aprons, which represent the most functionally and operationally critical elements of the airport infrastructure.

In **Step 5**, the HAZUS methodology [29] was employed to estimate the probability of liquefaction under a selected seismic scenario. A magnitude Mw 6.3 earthquake associated with the nearby Kavala-Xanthi-Komotini fault system was chosen. Ground motion modelling was performed using REDAS software [63], based on input from the SHARE and GreDaas databases [64,65], producing a peak ground acceleration (PGA) value of 0.36 g. Scenario fault rupture is considered as

representative of strong onshore earthquakes in continental Greece, while these PGA values represent site surface conditions, using  $V_{s30}$  grid (Greece  $V_{s30}$  model developed by Stewart et al. [66] using local geological and geotechnical data) and weighted GMPEs from Chiou and Youngs [67] and Boore et al. [68]. They are also compatible with the 955-year return period results of the seismic hazard model of Thrace developed by Sotiriadis et al. [69]. Groundwater depth in the area of the airport was evaluated using a delta-wide borehole dataset derived from hydrogeological surveys conducted in 1978, complemented by more recent observations from the 2014 groundwater survey in the eastern part of the region [70–73]. The latter indicates that the piezometric surface of the phreatic/unconfined aquifer has risen in recent years, likely due to the abandonment of shallow boreholes and the adoption of surface irrigation and deeper boreholes [73]. Considering these datasets, along with the known seasonal saturation patterns of the Holocene alluvial, fluvial, and coastal sediments that dominate the study area, groundwater depth was estimated to be generally less than 6 m. Given this input and the moment magnitude the conditional probability of liquefaction was calculated for each susceptibility class, classifying the

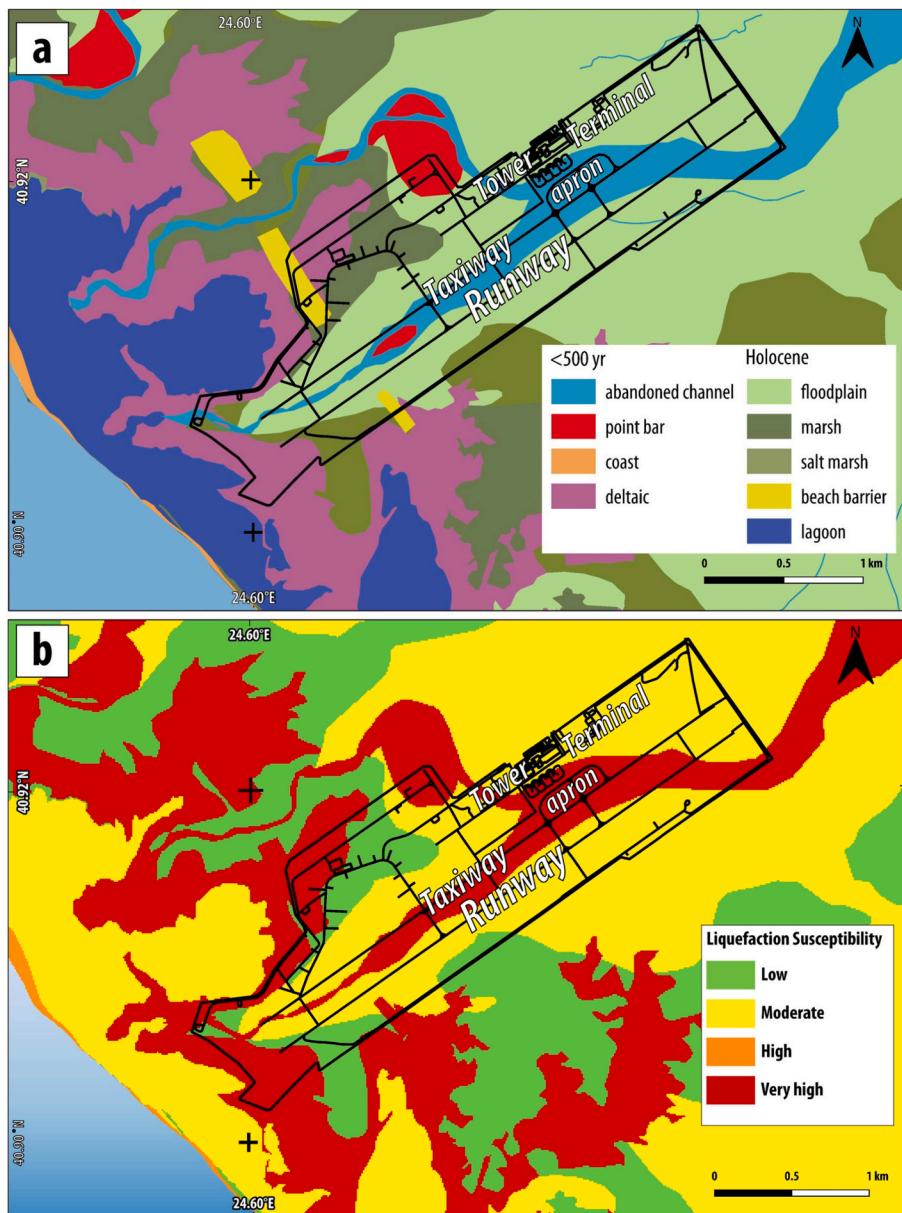


Fig. 4. (a) The new geomorphological map of surficial geological units and (b) the liquefaction susceptibility map for the area of KVA.

site into four probability zones.

In **Step 6**, expected ground settlements PGD were estimated as the product of probability of liquefaction (PLsc) and the characteristic ground settlement amplitudes corresponding to each susceptibility class (Table 2). Emphasis was placed on zones of moderate to very high susceptibility, which overlap with critical airport infrastructure. Due to the inactivity of the surrounding channels and the lack of geomorphological features (i.e. point-bars), conducive to lateral spreading; the potential of liquefaction-induced horizontal deformation was considered negligible in the case of KVA.

**Step 7** focused on assessing the vulnerability and expected losses associated with the estimated PGD values. The analysis concentrated on key airport components such as runways, taxiways, and apron areas. PGD was used as the hazard intensity measure to estimate the probability of exceeding slight-to-moderate, extensive, and complete damage levels, following the fragility functions and damage state thresholds defined in HAZUS [29]. Average damage ratios of 0.10, 0.40, and 0.80 were applied for each damage level respectively based on ranges of damage ratios proposed by HAZUS (Table 3). These were used to derive

average loss ratios for each susceptibility class [61], and, in turn, to compute the expected direct losses. Final loss estimations accounted for the affected area and the unit reconstruction costs of the relevant airport infrastructure.

Finally, in **Step 8**, the integrated outputs were used to produce a spatial risk profile for KVA, highlighting the most vulnerable zones of the airport under the selected earthquake scenario. This final step supports informed decision-making for inspection prioritisation, risk communication, and the development of targeted mitigation measures tailored to critical airport assets.

## Results

Based on the spatial distribution of surficial geological units derived from the geomorphological mapping, the application of Youd and Perkins [40] criteria resulted in the classification of the KVA area into four liquefaction susceptibility classes: low, moderate, high, and very high (Fig. 4). Overlaying the airport infrastructure on this map revealed that approximately 300 m of the northwestern runway, 2.7 km of the

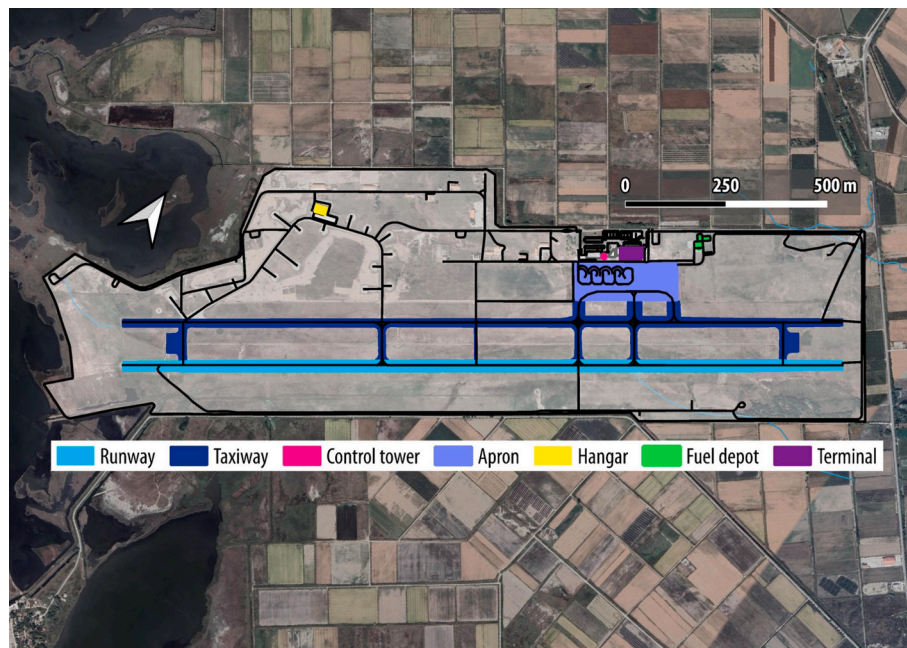


**Fig. 5.** Critical components of KVA airport collected from Google Maps and Open Street Maps according to Step 4.

**Table 3**  
Damage ratios for airport runways.

Damage State	Best Estimate Damage Ratio	Range of Damage Ratios
Slight	0.10	0.01 to 0.15
Moderate	0.40	0.14 to 0.40
Extensive	0.80	0.40 to 0.80
Complete	1.00	0.80 to 1.00

adjacent taxiway, and 78 m<sup>2</sup> of the apron are located on an abandoned river branch—an area classified as very high susceptibility to liquefaction. The remaining facilities were predominantly situated on moderately susceptible floodplain deposits.

Using the HAZUS methodology [29], the conditional probability of liquefaction for each susceptibility class under the selected seismic scenario (Mw 6.3, PGA = 0.36 g, groundwater depth < 6 m) was estimated (Step 5). The calculated probabilities were: 0.20 for very high, 0.16 for high, 0.08 for moderate, and 0.03 for low susceptibility areas (Table 4, Fig. 6). The corresponding expected permanent ground displacements (PGD) were computed by multiplying the probability of liquefaction by the characteristic settlement amplitude for each class. The results indicated average PGD values of 6.10 cm, 2.40 cm, 0.40 cm, and 0.10 cm for the very high, high, moderate, and low susceptibility classes, respectively (Table 4, Fig. 6).

Given that critical airport infrastructure (runway, taxiway, apron) is located within moderate to very high susceptibility zones, these PGD estimates were used as intensity measures for evaluating damage probabilities in Step 7. The following PGD ranges were used: 0.2–0.8 cm for moderate zones and 3.1–12.3 cm for very high zones. These values

were applied to estimate the probability of exceeding various damage states—slight/moderate, extensive, and complete—using HAZUS-defined fragility functions. The average loss ratios associated with PGD values of 6.1 cm and 0.4 cm were calculated as 0.1534 and 0.0004, respectively.

In Step 7, these were used to compute direct losses by multiplying the loss ratios with the area of each infrastructure component and the corresponding reconstruction cost per m<sup>2</sup>. The following reconstruction costs were considered: €186/m<sup>2</sup> for asphalt-paved runway (3,000 × 45 m<sup>2</sup>), €164/m<sup>2</sup> for taxiway (4,000 × 35 m<sup>2</sup>), and €164/m<sup>2</sup> for apron (96,000 m<sup>2</sup>). Reconstruction costs (Table 5) were derived from the airport pavement cost tables of [74]. The 2011 U.S. values were updated to 2024 using inflation indices and adjusted to the Greek context using PPP factors. As shown in Table 5, the estimated direct losses were €0.37 million for the runway, €2.5 million for the taxiway, and €2.0 million for the apron, leading to a total expected loss of approximately €5 million for the defined seismic scenario. Loss ranges reflect the variation in PGD and associated damage states across the different susceptibility zones.

The spatial risk profile for KVA enables targeted inspection planning and resilience measures (Step 8), focusing on infrastructure segments located in areas of high liquefaction susceptibility and ground deformation. This facilitates prioritisation of mitigation measures, including soil stabilisation or drainage improvements, particularly in zones underlain by abandoned river channels and deltaic deposits. The framework also supports scenario-based assessments, allowing comparisons across different earthquake magnitudes or fault sources, as well as other threats for enhancing long-term resilience planning [75] by airport operators, insurers and investors.

**Table 4**  
Estimated liquefaction probabilities and ground settlements (PGD) based on HAZUS methodology. The moment magnitude (K<sub>M</sub>) and groundwater (K<sub>W</sub>) correction factors are: K<sub>M</sub> = 1.2, K<sub>W</sub> = 1.0.

Susceptibility Class	P[Liquefaction <sub>sc</sub>  PGA = a]	P <sub>ml</sub>	P <sub>Lsc</sub>	PGD amplitude (cm)	Expected PGD (cm)	Range (cm)
Very High (VH)	0 ≤ 9.09a – 0.82 ≤ 1.0	0.25	0.20	30.50	6.10	3.10–12.30
High (H)	0 ≤ 7.67a – 0.92 ≤ 1.0	0.20	0.16	15.20	2.40	1.20–4.90
Moderate (M)	0 ≤ 6.67a – 1.0 ≤ 1.0	0.10	0.08	5.10	0.40	0.20–0.80
Low (L)	0 ≤ 5.57a – 1.18 ≤ 1.0	0.05	0.03	2.50	0.10	0.00–0.20

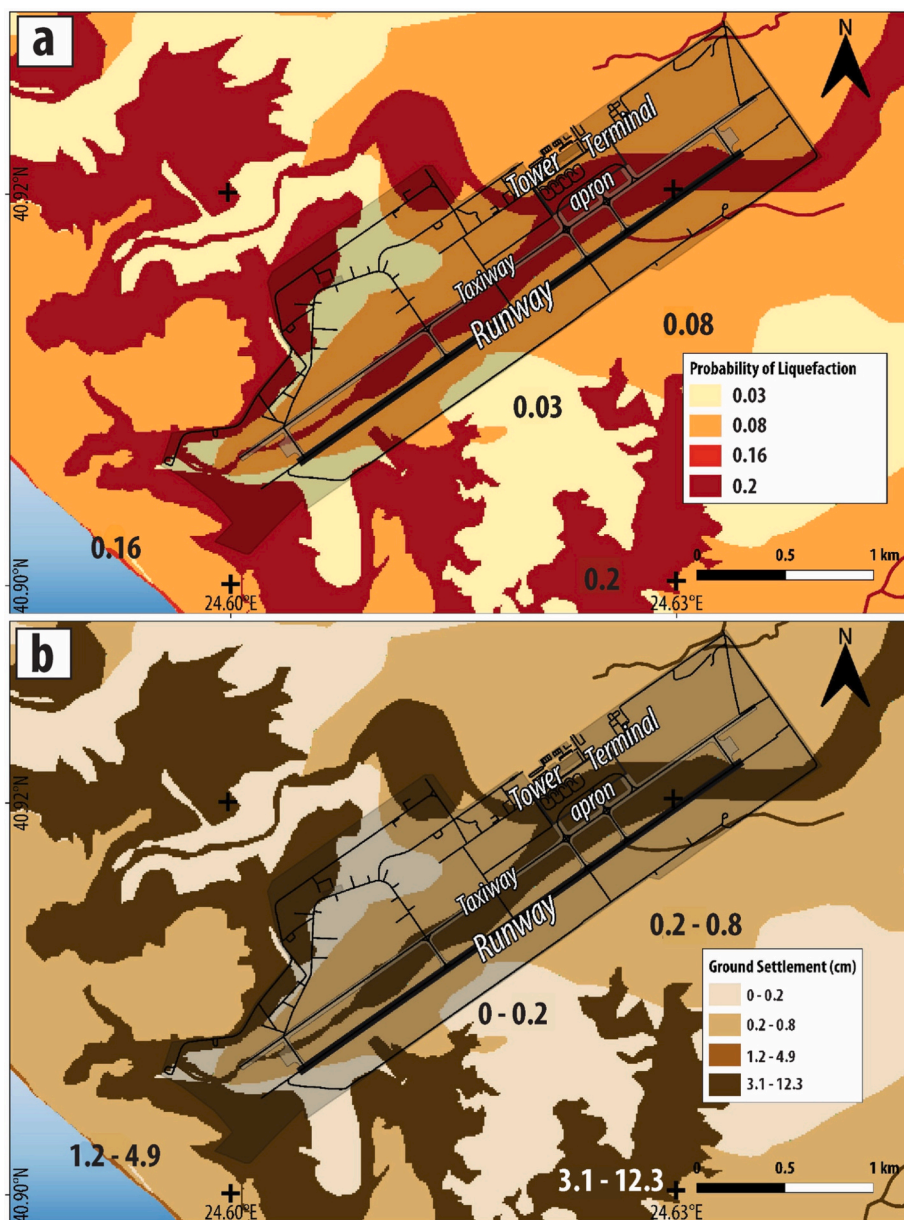


Fig. 6. (a) Probability of liquefaction and (b) expected ground settlements in KVA area.

**Table 5**  
Estimated direct losses for KVA airport infrastructure.

Facility	PGD (cm)	Area (m <sup>2</sup> )	Avg. loss ratio	Reconstruction cost (€/m <sup>2</sup> )	Direct loss (€)	Loss range (€)
Runway	0.2–0.8	122,247	0.0004	186	8,300	0–50,900
	3.1–12.3	12,753	0.1534	186	363,400	162,700–737,100
Taxiway	0.2–0.8	45,513	0.0004	164	2,728	0–16,700
	3.1–12.3	99,489	0.1543	164	2,534,000	1,100,000–5,100,000
Apron	0.2–0.8	17,605	0.0004	164	1,100	0–6,500
	3.1–12.3	78,468	0.1534	164	1,900,000	883,900–4,000,000
Total					€5.0 million	€2.2–€9.9 million

#### Validation

Historical earthquake events—including the 1989 Loma Prieta

(USA), 2001 Nisqually (USA), and 2023 Turkey–Syria earthquakes—have highlighted the vulnerability of airports to secondary seismic hazards such as soil liquefaction. In particular, Oakland

International Airport (OAK), King County International Airport (BFI), and Hatay International Airport (HTY) experienced extensive damage, including pavement cracking, subsidence, and ground surface discontinuities. To validate the methodology applied at Kavala International Airport (KVA), a comparative analysis was conducted using available data from these past events. The HAZUS framework was used to simulate liquefaction susceptibility and associated risk at each airport, allowing for a benchmark comparison with the KVA results and demonstrating the applicability and reliability of the proposed approach.

It should be acknowledged that HAZUS was originally developed for U.S. conditions, which introduces uncertainties when applying its soil parameters, liquefaction probability factors (KM, KW, Pml), or settlement amplitudes to other regions. However, these formulations are based on empirical relationships widely used internationally, and their transferability is supported here through validation at three well-documented liquefaction-affected airports (OAK, BFI, HTY). In all cases, the predicted susceptibility, liquefaction probability, and PGD ranges showed strong consistency with observed field displacements, indicating that HAZUS can provide reliable regional-scale screening in diverse sedimentary settings. Nonetheless, we recognise that site-specific applications would benefit from future calibration using local CPT/SPT and groundwater data.

#### Oakland International Airport (OAK)

Oakland International Airport (OAK) is situated along the eastern shore of San Francisco Bay in western Alameda County. Geological and historical maps indicate that the airport is built across former tidal marshes, tidal flats, and shallow bay environments (SFEI, 2000). Sub-surface materials primarily consist of Holocene estuarine deposits, Holocene and Pleistocene alluvial deposits, and the late Pleistocene to early Holocene Merritt Sand [43,76,77]. The northeastern portion of the airport, which represents the original facility footprint, lies over marshland influenced by deltaic and stream channel deposits from San Leandro Creek. Conversely, the southwestern section is constructed on fill placed over former tidal flats and shallow bay muds. The artificial fill consists of loose to dense sand, silty sand, and stiff to medium stiff silt and clay, with variable gravel content. Its thickness ranges from 2.5–4 m in the southern sector to 0.3–2 m in the north [78].

On October 17, 1989, the Mw 6.9 Loma Prieta earthquake struck approximately 80 km from the OAK site, triggering widespread liquefaction across the Bay Area and causing significant damage to airport infrastructure. One of the most affected facilities was the 3-km main runway (11–29), built on hydraulic fill over Bay mud. Approximately 900 m of its northwestern section exhibited sand boils, pavement buckling, and vertical and lateral displacements of 20 cm and 60 cm, respectively [79]. The western end of the runway was also laterally

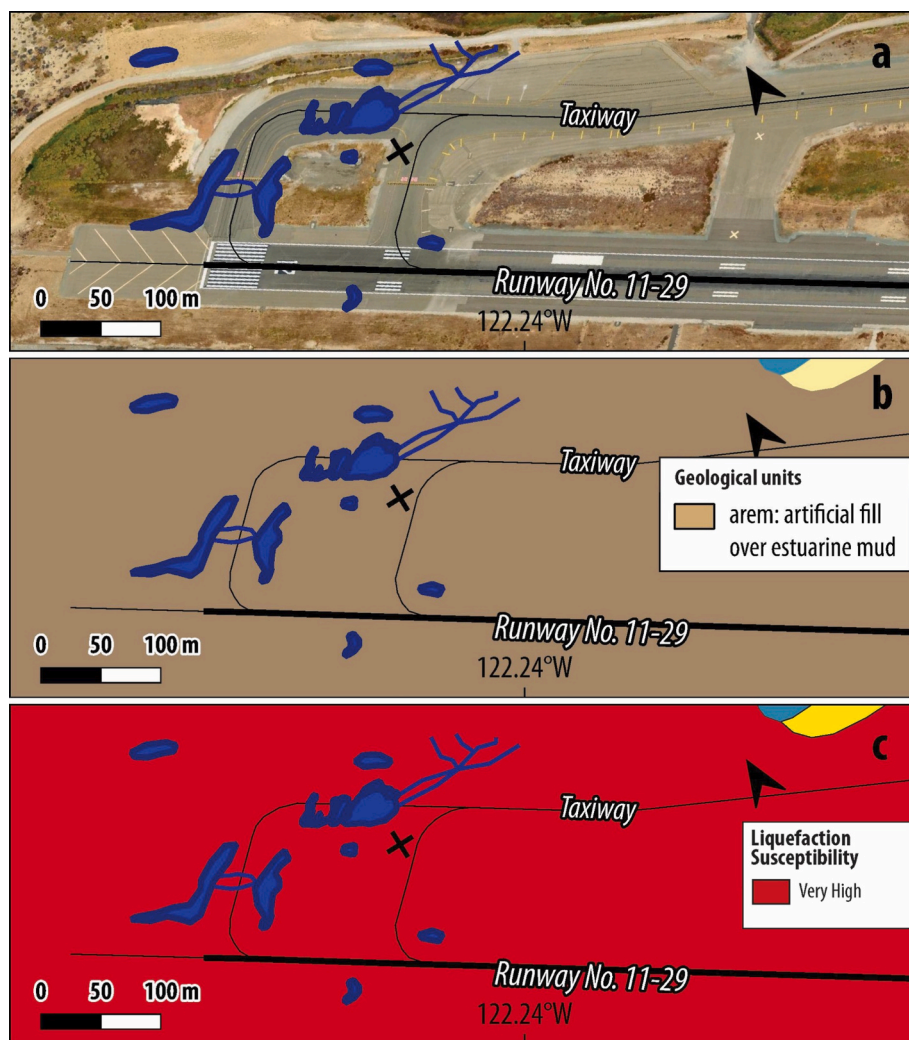


**Fig. 7.** Liquefaction ejecta and ground cracking (blue zones) at OAK following the 1989 Loma Prieta earthquake, projected onto: (a) satellite imagery, (b) geological units map, and (c) liquefaction susceptibility map (modified after [80]). (For interpretation of the references to colour in this figure legend, the reader is referred to the web version of this article.)

shifted by about 60 cm, while the adjacent taxiway sustained 30 cm pavement cracks and 15 cm of vertical settlement [15]. Ground cracks and liquefaction ejecta zones, with typical lengths of up to 70 m, were documented (Fig. 7, Fig. 8).

The primary factors contributing to these failures included the shallow water table, uniform gradation of fill material, and the presence of saturated, relatively loose sand layers beneath the fill. Additional liquefaction effects were reported at the main terminal building, where sand intrusion was observed in an annex, and at a nearby taxiway, which experienced settlements of up to 8 cm [14,15]. The total repair costs were approximately \$3.5 million for the runway and \$2.2 million for the taxiway [81].

Application of the HAZUS methodology to the OAK site showed strong consistency with these observed impacts. The resulting liquefaction susceptibility map classified most of the airport as highly susceptible, and the HAZUS-based analysis estimated a probability of liquefaction of 0.22, with expected ground settlements ranging from 3.40 to 13.60 cm (Table 6; Fig. 8). These outcomes closely align with the recorded displacements and field damage reports, supporting the validity of the applied methodology.

#### King County International Airport (BFI)

King County International Airport (BFI), also known as Boeing Field, is located within the Duwamish River corridor, south of downtown Seattle, Washington. The area has undergone extensive anthropogenic modification, particularly between 1890 and 1930, during which time natural features such as meanders, tidal flats, depressions, and the river mouth were filled through hydraulic placement [82]. The airport is situated on Quaternary alluvial sediments, with parts of its infrastructure—most notably sections of the runway—constructed over abandoned meander channels, which are known to have elevated liquefaction potential. Following the Mw 6.8 Nisqually earthquake in 2001, BFI experienced widespread liquefaction [20,83].

Application of the HAZUS methodology indicated that BFI

predominantly falls within the high susceptibility class, with a liquefaction probability of 0.08, while the portion of the runway situated on the abandoned meander was classified as very high susceptibility, with an estimated probability of 0.17. The corresponding ground settlement estimates ranged from 0.60 to 2.30 cm in high susceptibility zones, and from 2.50 to 10.20 cm in the very high zones. The spatial projection of affected areas onto susceptibility, probability, and settlement maps confirmed a high degree of consistency between HAZUS-based predictions and observed field damage (Table 6, Fig. 9).

Liquefaction effects were most pronounced along the eastern runway, where sand ejecta fields extended approximately 90 m, and ground surface settlements reached up to 20 cm. In contrast, the western runway was impacted by only a few isolated sand boils. Notably, the northern portion of the airfield experienced the formation of a sinkhole approximately 1.2 m wide and 1.8 m deep. These features were attributed to cyclic ground oscillations, which also resulted in pavement cracking at the joints along both runways. A particularly significant longitudinal crack, measuring nearly 305 m in length and 1.2 to 2.5 cm in width, was observed along the western edge of the western runway. The spatial distribution of these manifestations closely followed the course of a former Duwamish River meander, reinforcing the importance of geomorphological history in assessing liquefaction vulnerability.

#### Hatay International Airport (HTY)

HTY is located in the western Amik Plain, on the former lakebed of Amik Lake [85]. The geological setting reflects significant lacustrine and fluvial influences, with the lake's floor now consisting predominantly of fine-grained sediments—including silts of low to medium plasticity with varying clay content—extending to depths of up to 30 m [86]. Following the 2023 Türkiye–Syria earthquake doublet—which involved two major earthquakes (Mw 7.7 and Mw 7.6) along the East Anatolian Fault Zone (EAHZ)—HTY experienced both surface rupture and liquefaction-induced ground displacements (Fig. 7). In the western

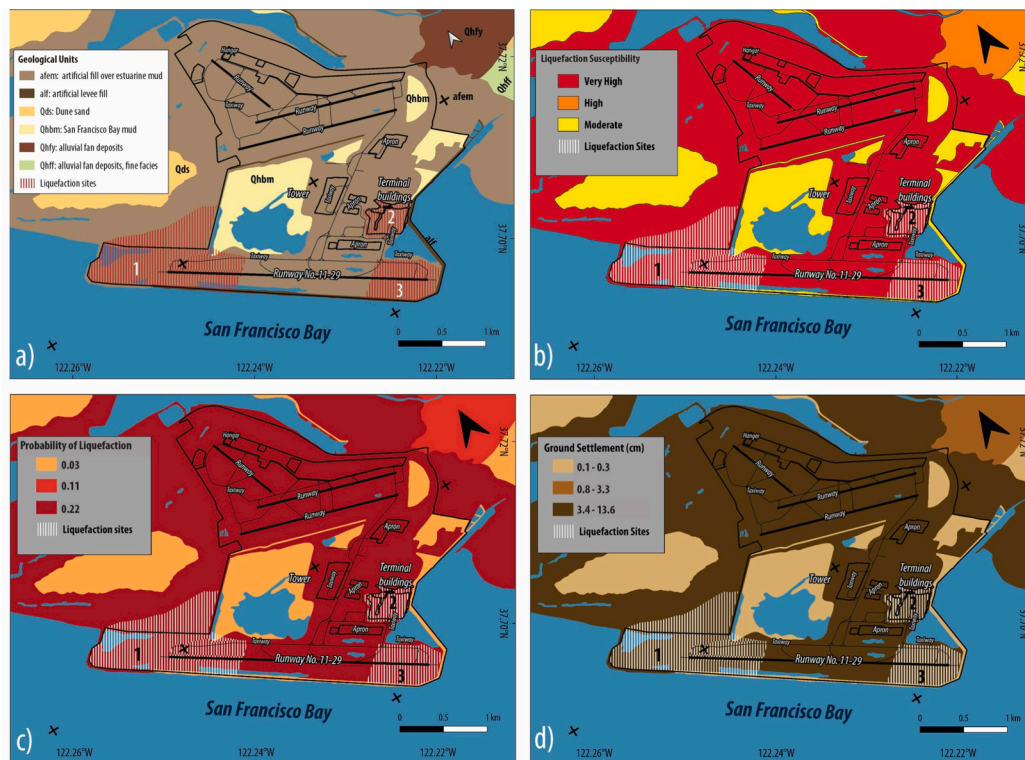


**Fig. 8.** Liquefaction manifestations at OAK based on: (a) geological units, (b) liquefaction susceptibility, (c) liquefaction probability, and (d) ground settlement (modified after [43]).

**Table 6**

Estimation of liquefaction probability (PLsc) and expected permanent ground displacement (PGD) for KVA, OAK, BFI, and HTY airports, based on the FEMA [29] methodology and categorised by susceptibility class (SC). Asterisks (\*) indicate susceptibility classes that intersect directly with critical airport infrastructure (e.g. runways, taxiways, aprons).

Earthquake	KVA (scenario)	OAK (17/09/1989)	BFI (28/02/2001)	HTY (06/02/2023)
PGA (g)	0.36	0.20	0.18	0.80
Mw	6.30	6.90	6.80	7.70
K <sub>W</sub>	1.00	1.00	1.10	1.10
K <sub>M</sub>	1.20	1.10	1.10	1.00
SC Class	PLsc			P <sub>ml</sub>
Very High (VH)	0.20*	0.22*	0.17*	0.24*
High (H)	0.16	0.11*	0.08*	0.19
Moderate (M)	0.08*	0.03*	0.02	0.10
Low (L)	0.03*	0.00	0.00	0.05
SC Class	Expected PGA (cm)			PGD (settlement) amplitude (cm)
Very High (VH)	3.10–12.30*	3.40–13.60*	2.50–10.20*	3.60–14.40*
High (H)	1.20–4.90	0.80–3.30*	0.60–2.30*	1.40–5.70
Moderate (M)	0.20–0.80*	0.10–0.30*	0.00–0.20	0.20–1.00
Low (L)	0.00–0.20*	0.00	0.00	0.10–0.20

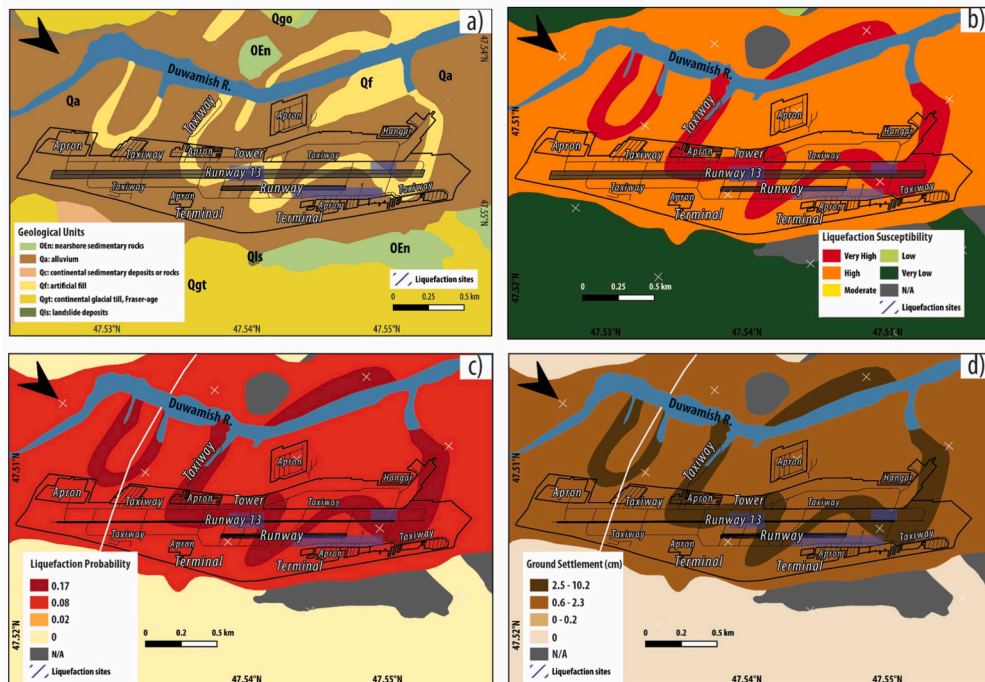


**Fig. 9.** Liquefaction manifestations of the 2001 Nisqually earthquake at BFI Airport, based on maps of: (a) geological units, (b) liquefaction susceptibility, (c) liquefaction probability, and (d) ground settlement (modified after [84]).

section of the airport, a series of ground cracks oriented southwest were observed, attributed to a surface rupture along a previously unmapped segment of the Dead Sea Fault Zone (DAFZ) [21]. The surface ruptures may have facilitated the upward movement of liquefied material, contributing to the formation of sand ejecta. Given the combination of strong ground shaking and the mechanical properties of the underlying fine-grained sediments, the HTY site was particularly prone to deformation. Furthermore, as observed in the 1999 Kocaeli earthquake [87], the development of surface ruptures may have been influenced by differential settlement, likely resulting from variations in sediment thickness between the eastern and western parts of the airport.

In contrast, the eastern part of the airport exhibited classic liquefaction and shaking-induced deformation. Field surveys documented vertical displacements of 30–40 cm and horizontal shifts of 10–15 cm [86]. These ground movements, along with visible cracks and craters on the runway and adjacent infrastructure, resulted in the closure of the

airport for six days. Detailed inspection revealed 12 transverse ground cracks with associated sand ejecta on the runway, and an additional seven liquefaction sites on the central taxiways and apron (Fig. 11). The average length of runway cracks was 45 m, with a regular spacing pattern of approximately 100 m in the middle section and 150 m in the eastern part.

The spatial projection of these field observations onto the HAZUS based – generated maps confirmed the accuracy of the methodology. Nearly the entire airport infrastructure was classified as very highly susceptible to liquefaction, with an estimated liquefaction probability of 0.24 and expected ground settlements ranging from 3.60 to 14.40 cm (Table 6, Fig. 10). The alignment between observed damage and modelled outputs provides additional confidence in the methodology's applicability to data-sparse, geologically sensitive regions like HTY.

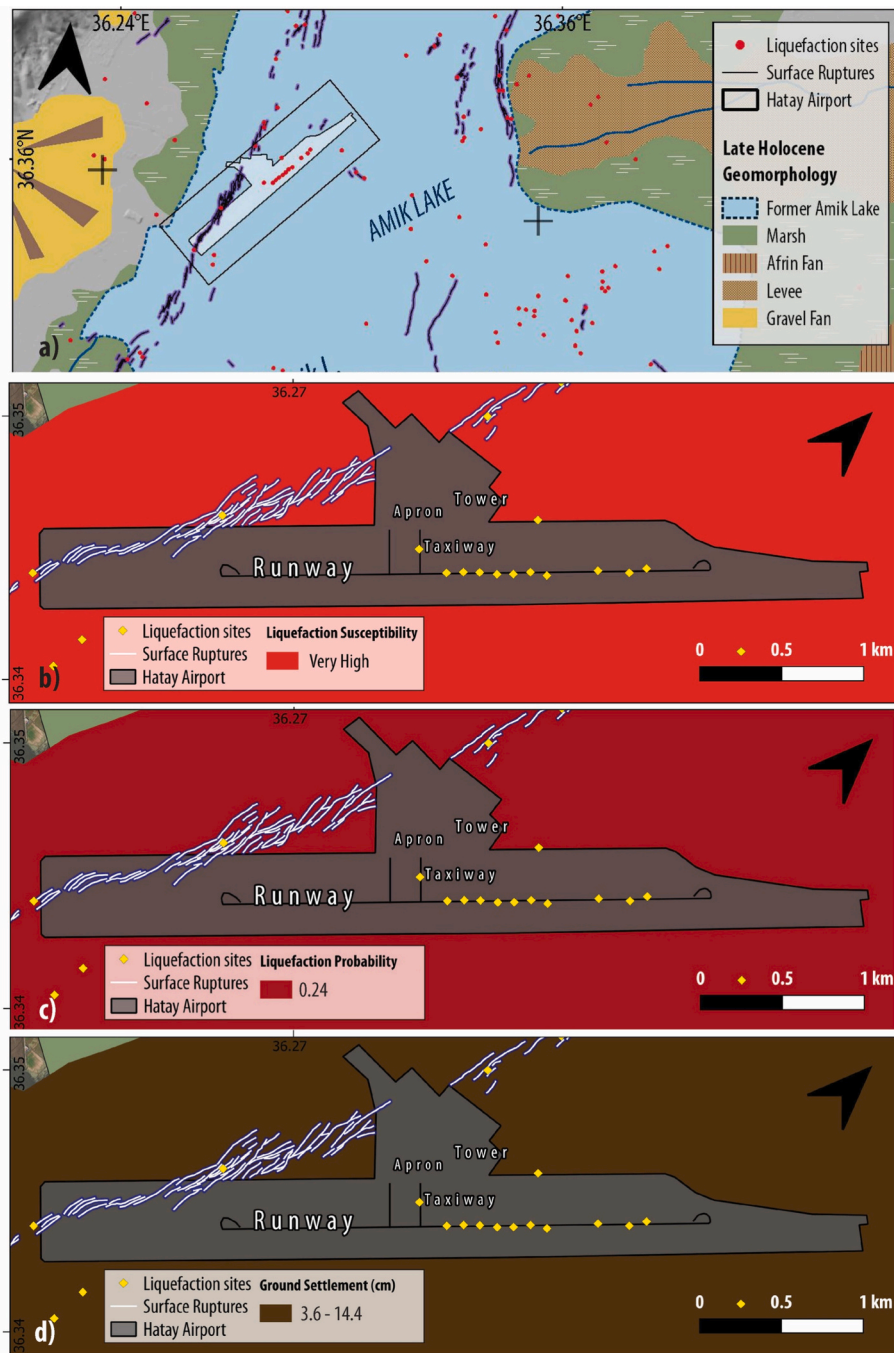


**Fig. 10.** Liquefaction manifestations of the 2023 Türkiye–Syria earthquake doublet at HTY Airport, based on maps of: (a) geological units (modified after [21]), (b) liquefaction susceptibility, (c) liquefaction probability, and (d) ground settlement.

## Discussion

The cases of OAK, BFI, and HTY airports represent well-documented examples of liquefaction-induced damage to critical transportation infrastructure. These datasets were instrumental in validating the methodology proposed in this study. A comparison of observed and predicted outcomes revealed that liquefaction manifestations consistently occurred within areas classified as “very high susceptibility” by the HAZUS-based framework. This supports the reliability of the susceptibility mapping and risk estimation approach. However, the extent of observed damage was generally more localised than the predicted susceptible zones. This discrepancy highlights the influence of data availability and spatial resolution on validation outcomes. For OAK and

BFI, damage was documented as generalised zones of liquefaction, while in HTY, liquefaction manifestations were reported as specific discrete sites. This difference in documentation scale introduced a level of qualitative comparison, rather than precise spatial matching between observed and predicted extents.

Across both the KVA case study and the three validation airports (OAK, BFI, HTY), the spatial patterns of predicted PGD consistently align with operationally sensitive pavement nodes such as runway–taxiway intersections, turning segments, and apron transition zones. These areas coincide with underlying geomorphological weaknesses—abandoned channels, reclaimed tidal flats, and fine-grained lacustrine deposits—where liquefaction-induced settlement tends to localise. Even moderate PGD levels can affect braking efficiency, pavement evenness, and safe



**Fig. 11.** Satellite view of the HTY airport area. Yellow and red index zones indicate: (a) surface ruptures located on the western side of the runway, and (b) transverse ground cracks and sand ejecta observed along the central and eastern sections of the runway and parts of the taxiway (modified after [86]. (For interpretation of the references to colour in this figure legend, the reader is referred to the web version of this article.)

aircraft manoeuvring, while higher PGD concentrations may necessitate temporary closure or traffic restrictions. The consistency of these patterns across four international airports highlights the practical value of PGD mapping not only for damage estimation but also for identifying critical points where liquefaction-related deformation is most likely to impair airport operability.

Given the airport runway is both functionally critical and, as shown in all three cases, highly vulnerable to liquefaction, this component was selected as a focal point for spatial comparison. The correlation between predicted and observed runway failures is presented in Table 7 and summarised in Fig. 12.

- At OAK, the runway lies entirely within the very high susceptibility zone. Observed damage affected approximately 53.4 % of the total predicted susceptible area, indicating a relatively strong match between modelled and observed impact.
- At BFI, the runway spans both very high and high susceptibility zones. The total predicted liquefiable area was estimated at  $3.8 \times 10^5$  m<sup>2</sup>, yet only  $0.37 \times 10^5$  m<sup>2</sup> was reported as affected—representing 18.2 % and 5.8 % of the very high and high zones, respectively. This

partial correlation reflects the spatial heterogeneity of the liquefaction process and possibly unreported minor manifestations. Liquefaction is often patchy, controlled by local soil layering, groundwater variations, and non-uniform cyclic stress levels—factors that static surrogate models like HAZUS may not capture [25].

- At HTY, the entire runway falls within the very high susceptibility class. While the model predicted failure over an area of  $1.85 \times 10^5$  m<sup>2</sup>, only  $0.06 \times 10^5$  m<sup>2</sup> (approximately 3.2 %) was documented as affected. This can be attributed to the coarse granularity of the data—damage reports were limited to discrete “sites” rather than continuous zones, unlike the zone-based observations at OAK and BFI—and to the high spatial variability in sediment characteristics and groundwater depth. Similar discrepancies between predicted and observed extents have been noted in regional liquefaction studies, where fine-scale heterogeneity leads to over-prediction by geospatial models.

To incorporate quantitative spatial validation, we computed the overlap area between the predicted liquefaction-susceptible runway zones (VH or VH + H) and the mapped footprints of observed

**Table 7**

Quantitative validation of predicted (PR) versus observed (OB) liquefaction-induced runway failures for OAK, BFI, and HTY airports. The table reports the overlap area and derived performance indicators—True Positive Rate (TPR), Precision, and Intersection-over-Union (IoU)—to assess spatial agreement between predicted susceptible zones and mapped damage extents. Asterisks (\*) indicate combined totals for the very high (VH) and high (H) susceptibility classes at BFI.

Airport	SC	PR failures ( $\times 10^5$ m <sup>2</sup> )	OB failures ( $\times 10^5$ m <sup>2</sup> )	OB failures (%)	Precision (%)	IoU	TPR
OAK	VH	2.81	1.50	53.40	53.40	0.53	1.00
BFI	VH	1.21	0.22	18.20	18.20	0.82	1.00
	H	2.59	0.15	5.80	5.80	0.06	1.00
	VH + H	3.80*	0.37*	24.00*	24.00*	0.10*	1.00
HTY	VH	1.85	0.06	3.20	3.20	0.03	1.00

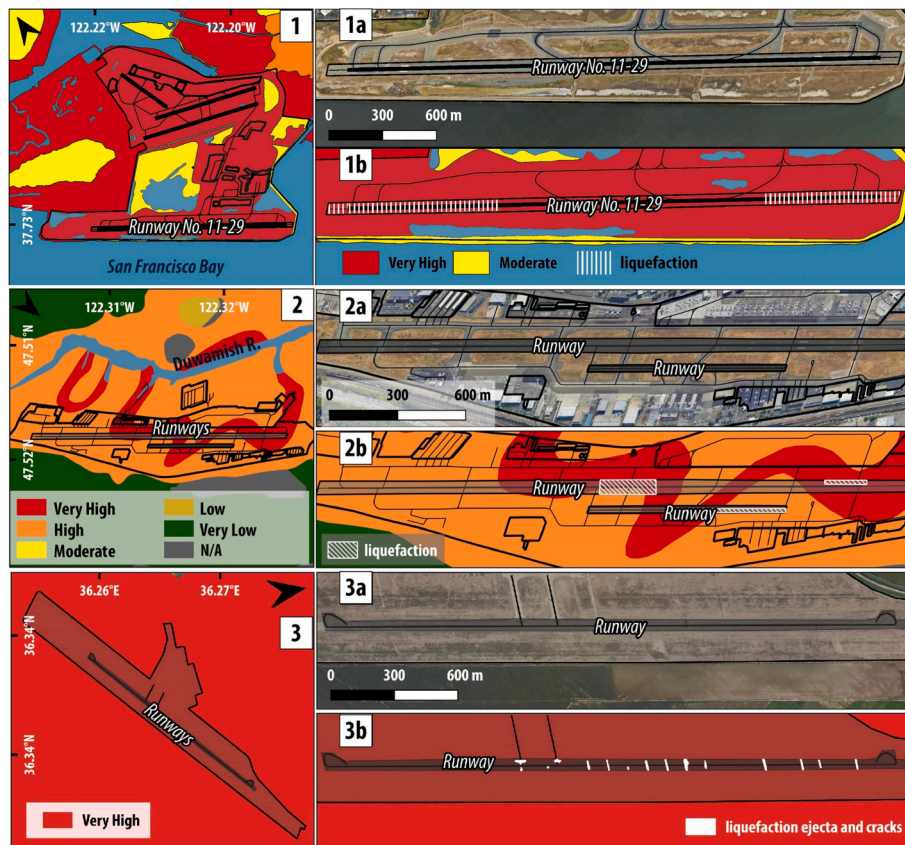


**Fig. 12.** Liquefaction susceptibility classes overlaid with observed liquefaction records along the runways of: (1) Oakland International Airport (OAK), (2) King County International Airport (BFI), and (3) Hatay International Airport (HTY). The figure highlights the spatial correspondence between predicted susceptibility zones and recorded liquefaction damage.

liquefaction damage at OAK, BFI, and HTY. In all three cases, the observed failures were entirely contained within the predicted susceptible areas, meaning that the overlap area equals the observed area. Based on this intersection, three performance indicators were derived: (i) True Positive Rate (TPR), defined as the overlap area divided by the total observed damaged area ( $TPR = \text{overlap}/\text{observed}$ ); (ii) Precision, defined as the proportion of the predicted susceptible area that corresponds to observed failures ( $\text{Precision} = \text{overlap}/\text{predicted}$ ); and (iii) Intersection-over-Union (IoU), which measures spatial agreement between predicted and observed extents ( $\text{IoU} = \text{overlap}/(\text{predicted} + \text{observed} - \text{overlap})$ ). These indicators, reported in Table 7, show high spatial consistency at OAK and BFI (higher Precision and IoU values) and lower agreement for HTY, reflecting the smaller and more localised nature of observed manifestations there.

These findings underline the importance of data resolution, geomorphological variability, and ground investigation density in validating susceptibility models. Despite these limitations, the results demonstrate that the proposed methodology provides a robust framework for identifying high-risk areas and supporting prioritised mitigation planning. Yet, the observed discrepancies described above highlight the necessity of interpreting susceptibility and risk maps as first-pass screening tools. For infrastructure planning, overlaying predicted zones with targeted site investigations (e.g., CPT, shear-wave velocity) is essential to refine risk assessments [88]. Moreover, adopting probabilistic models that incorporate geotechnical variability can yield more accurate, site-specific predictions.

## Conclusions

This study presents a scalable and rapid framework for assessing airport infrastructure risk due to seismic-induced soil liquefaction, by

integrating multi-modal data sources—including geological maps, remote sensing imagery, digital elevation models, and open-access infrastructure data. The proposed nine-step methodology offers a data-efficient and reproducible approach to identifying and quantifying liquefaction susceptibility, ground deformation, and potential losses in critical airport assets. The methodology was applied to Kavala International Airport (KVA) in northern Greece. Using remote sensing and geological datasets, a geomorphological base map was developed and used to classify surficial units by age and depositional environment. Liquefaction susceptibility was mapped using Youd and Perkins [40] criteria, identifying very high and moderate susceptibility zones that coincide with major airport components such as the runway, taxiway, and apron. Based on a representative seismic scenario (Mw 6.3), the probability of liquefaction was estimated as 0.2 for the most critical zones, with expected ground settlements (PGD) reaching 6.1 cm. Total direct losses were estimated at €5 million, with the taxiway and apron accounting for the largest share.

Validation using historical earthquake cases at Oakland (OAK), King County (BFI), and Hatay (HTY) International Airports confirmed the method's reliability: observed damage aligned with areas predicted to be highly susceptible to liquefaction. However, the spatial extent of observed damage was more localised than predicted, due to factors such as subsurface heterogeneity, groundwater variability, shaking intensity, and differences in data resolution. Notably, at HTY, the limited spatial footprint of documented failures reflected the granularity of point-based field reports, as opposed to the zone-based data available at OAK and BFI.

This framework offers a risk screening tool that can be applied at national, regional, or global scales to assess critical airport infrastructure located in liquefaction-prone areas, particularly within coastal zones. By integrating multi-modal datasets—including geomorphological, remote

sensing, and open-access infrastructure data—it provides a practical, scalable solution for both data-rich and data-limited contexts. The methodology aligns with cascading hazard perspectives [89], where liquefaction may interact with or be compounded by hazards such as flooding, sea-level rise, and infrastructure interdependencies. Moreover, the framework is adaptable to climate-sensitive contexts, where sea-level rise and increased groundwater levels can elevate the probability and severity of liquefaction. In this way, it contributes to a broader understanding of the airport as a resilient ecosystem [90], by linking physical risk assessment with operational preparedness and strategic planning. The approach enables stakeholders to identify critical vulnerabilities, prioritise mitigation, and support long-term resilience, ultimately strengthening the capacity of airports to function under multiple, interacting stressors in an evolving Earth and climate system.

This study has some limitations that should be acknowledged. One constraint is that the HAZUS framework was originally calibrated for U.S. geological conditions and infrastructure typologies, which may differ from those present in other regions; although its empirical formulations for liquefaction triggering, settlement, and vulnerability are widely used internationally, regional variations in soil properties, groundwater regimes, and pavement design practices may influence accuracy. The multi-site validation across three airports helps mitigate this limitation, demonstrating consistency between predicted susceptibility patterns, PGD ranges, and observed liquefaction manifestations.

An additional source of uncertainty arises from the liquefaction susceptibility map itself, which depends on the level of detail available in the geomorphological mapping of the study area. Because the delineation of geomorphological units influences the classification of susceptibility zones, minor variations may occur depending on the scale and resolution of the remote sensing and geological datasets originally used. These variations may affect the estimated liquefaction probability for the airport and, consequently, the predicted permanent ground deformations (PGD). To account for this uncertainty, the analysis includes proposed ranges of maximum and minimum expected settlement rather than relying on a single deterministic value.

Furthermore, limitations relate to the input groundwater and geomorphological datasets, which may not fully capture seasonal variability, long-term trends, or climate-driven changes, while post-event damage reporting varies in detail and spatial completeness. Future research should therefore prioritise improved hydrogeological and geomorphological datasets, integration of probabilistic seismic scenarios, and assessment of interactions with other hazards—such as flooding, sea-level rise, or subsidence—to enhance the framework's adaptability to multi-hazard and climate-sensitive contexts. Finally, expanding and testing the methodology across other critical infrastructure types, such as ports, highways, or railways, and in diverse tectonic and environmental settings would further strengthen its applicability as a regional- and global-scale screening tool.

#### CRediT authorship contribution statement

**Maria Taftsgolou:** Writing – review & editing, Writing – original draft, Visualization, Validation, Software, Resources, Methodology, Investigation, Formal analysis, Data curation, Conceptualization. **George Papathanassiou:** Writing – review & editing, Supervision, Resources, Project administration, Methodology, Investigation, Conceptualization. **Sotirios Valkaniotis:** Writing – review & editing, Validation, Software, Resources, Methodology, Investigation, Formal analysis, Conceptualization. **Sotirios Argyroudis:** Writing – review & editing, Writing – original draft, Visualization, Supervision, Project administration, Methodology, Conceptualization. **Stergios-Aristoteles Mitoulis:** Writing – review & editing, Methodology, Conceptualization.

#### Declaration of competing interest

The authors declare that they have no known competing financial

interests or personal relationships that could have appeared to influence the work reported in this paper.

#### Acknowledgements

The first three authors acknowledge support of this work by the project “Risk and Resilience Assessment Center–Prefecture of East Macedonia and Thrace-Greece.” (MIS 5047293) which is implemented under the Action “Reinforcement of the Research and Innovation Infrastructure”, funded by the Operational Programme “Competitiveness, Entrepreneurship and Innovation” (NSRF 2014-2020) and co-financed by Greece and the European Union (European Regional Development Fund). The last two authors received funding by the UK Research and Innovation (UKRI) under the UK Government’s Horizon Europe funding guarantee (EP/Y003586/1, EP/X037665/1). This is the funding guarantee for the European Union HORIZON-MSCA-2021-SE-01 Recharged-Climate-aware Resilience for Sustainable Critical and Interdependent Infrastructure Systems enhanced by Emerging Digital Technologies.

#### Data availability

Data will be made available on request.

#### References

- [1] Yesudian AN, Dawson RJ. Global analysis of sea level rise risk to airports. *Climate Risk Management* 2021;31:100266. <https://doi.org/10.1016/j.crm.2020.100266>.
- [2] Youd TL. Liquefaction, flow, and associated ground failure. U.S. Geological Survey Circular 688; 1973. U.S. Geological Survey 1973;12. <https://doi.org/10.3133/cir688>.
- [3] Knudsen KL, Bott J. Geologic and geomorphic evaluation of liquefaction case histories for rapid hazard mapping. *Seismol Res Lett* 2011;82(2):334–5.
- [4] Bastin S, Stringer ME, Green RA, Wotherspoon L, van Ballegooij S, Cox BR, et al. Geomorphological controls on the distribution of liquefaction in Blenheim, New Zealand, during the 2016 Mw7.8 Kaikoura Earthquake. In: *Geotechnical Earthquake Engineering and Soil Dynamics V*. Reston, VA: American Society of Civil Engineers; 2018. p. 264–72. Doi: 10.1061/9780784481455.026.
- [5] Bastin SH, Quigley MC, Bassett K. Paleoliquefaction in Christchurch, New Zealand. *Bull Geol Soc Am* 2015;127(9–10):1348–60.
- [6] Papathanassiou G, Ganias A, Valkaniotis S. Recurrent liquefaction-induced failures triggered by 2014 Cephalonia, Greece earthquakes: Spatial distribution and quantitative analysis of liquefaction potential. *Eng Geol* 2016;200:18–30. <https://doi.org/10.1016/j.enggeo.2015.11.011>.
- [7] Minarelli L, Amoruso S, Civico R, De Martini PM, Lugli S, Martelli L, et al. Liquefied sites of the 2012 Emilia earthquake: a comprehensive database of the geological and geotechnical features (Quaternary alluvial Po Plain, Italy). *Bull Earthq Eng* 2022;20:3659–97. <https://doi.org/10.1007/s10518-022-01338-7>.
- [8] Valkaniotis S, Rapti D, Taftsgolou M, Papathanassiou G, Caputo R. Geomorphological mapping for liquefaction likelihood: the Pinida Valley case study (central Greece). *Bulletin of Earthquake Engineering* 2024;22:5451–74. <https://doi.org/10.1007/s10518-024-01993-y>.
- [9] Geyin M, Maurer BW. Fragility functions for liquefaction-induced ground failure. *J Geotech Geoenviron Eng* 2020;146(12):04020142. [https://doi.org/10.1061/\(ASCE\)GT.1943-5606.0002416](https://doi.org/10.1061/(ASCE)GT.1943-5606.0002416).
- [10] Ramos A, Grima J, Iturrarán-Viveros U, Silva P. Mechanistic–empirical permanent deformation models. *Road Mater Pavement Des* 2020;21(8):2321–45. <https://doi.org/10.1016/j.roadmat.2019.07.003>.
- [11] Tan Y-Q, Fu Y-K, Li Y-L, Zhang C. Responses of snow-melting airfield rigid pavement under aircraft loads, temperature loads, and their coupling effects. *Transp Geotech* 2018;14:107–16. <https://doi.org/10.1016/j.trgeo.2017.11.006>.
- [12] Adler M, Petrat A, Jongeling A, Kiefer M, De Jong G, Behrem C, et al. The economic and social impact of European airports and air connectivity. *ACI EUROPE, SEO Amsterdam, Economics* 2024;Report No:978-90-5220-453-6.
- [13] H.T. Harvey & Associates. Airport Roadway Project Port of Oakland, Biotic Habitats and Wetlands Report. Prepared for Woodward-Clyde Consultants and the Port of Oakland; 1993.
- [14] Seed RB, Riemer M, Dickenson SE. Liquefaction of soils in the 1989 Loma Prieta Earthquake. In: *Proceedings of the International Conferences on Recent Advances in Geotechnical Earthquake Engineering and Soil Dynamics*, Vol. 9; 1991.
- [15] Holzer TL. The Loma Prieta, California, earthquake of October 17, 1989 – Liquefaction. U.S. Geological Survey Professional Paper 1551-B; 1998. 314 p.
- [16] Metropolitan Transportation Commission. Adapting to Rising Tides: Transportation Vulnerability and Risk Assessment Pilot Project Briefing Book; 2011. [https://mtc.ca.gov/sites/default/files/Rising\\_Tides\\_Briefing\\_Book.pdf](https://mtc.ca.gov/sites/default/files/Rising_Tides_Briefing_Book.pdf).
- [17] Earthquake Engineering Research Institute. Loma Prieta Reconnaissance Report. *Earthq Spectra* 1990;6(Suppl):97–283.

- [18] Schiff AJ, editor. Northridge Earthquake – Lifeline Performance and Post-Earthquake Response. Technical Council on Lifeline Earthquake Engineering Monograph No. 8, American Society of Civil Engineers; 1995. p. 227–235.
- [19] Earthquake Engineering Research Institute. The Kyogo-Ken Nanbu Earthquake – January 17, 1995 – Preliminary Reconnaissance Report. EERI, Oakland, California; 1995. p. 1, 72.
- [20] Bray JD, Sancio RB, Kammerer AM, Merry S, Rodriguez-Marek A, Khazai B, et al. Some observations of geotechnical aspects of the February 28, 2001 Nisqually Earthquake in Olympia, South Seattle, and Tacoma, Washington; 2001. <http://peer.berkeley.edu/nisqually/geotech>.
- [21] Taftosoglou M, Valkaniotis S, Papathanassiou G, Karantanellis E. Satellite imagery for rapid detection of liquefaction surface manifestations: the case study of Türkiye–Syria 2023 Earthquakes. *Remote Sens* 2023;15(17):4190. <https://doi.org/10.3390/rs15174190>.
- [22] Iwasaki T, Tokida K, Tatsuoka F, Watanabe S, Yasuda S, Sato H. Microzonation for soil liquefaction potential using simplified methods. In: Proceedings of the 3rd International Conference on Microzonation, Vol. 3, Seattle, USA; June 28 - July 1, 1982. p. 1319–1330.
- [23] Papathanassiou G. LPI-based approach for calibrating the severity of liquefaction-induced damages and for assessing the probability of liquefaction surface evidence. *Eng Geol* 2008;96(1–2):94–104. <https://doi.org/10.1016/j.enggeo.2007.10.005>.
- [24] van Ballegooij S, Malan P, Jacka ME, Lacrosse V, Leeves JR, Lyth JE. Methods for characterizing effects of liquefaction in terms of damage severity. In: 15th World Conference on Earthquake Engineering, Lisbon, Portugal; 2012.
- [25] Maurer BW, Green RA, Taylor ODS. Moving towards an improved index for assessing liquefaction hazard: Lessons from historical data. *Soils Found* 2015;55(4):778–87. <https://doi.org/10.1016/j.sandf.2015.06.010>.
- [26] Werner SD, Taylor CE, Cho S, Lavoie J-P, Huyck C, Eitzel C, et al. Redars 2 methodology and software for seismic risk analysis of highway systems. Special Report MCEER-06-SP08. Multidisciplinary Center for Earthquake Engineering Research, University at Buffalo; 2006.
- [27] Pitilakis K, Crowley H, Kaynia AM. SYNER-G: Typology definition and fragility functions for physical elements at seismic risk. *Geotech Geol Earthq Eng* 2014;27:1–28.
- [28] D'Apuzzo M, Evangelisti A, Modoni G, Spacagna R-L, Paoletta L, Santilli D, et al. Simplified approach for liquefaction risk assessment of transportation systems: Preliminary outcomes 2020;1–4:130–45.
- [29] FEMA. Hazus Earthquake Model Technical Manual, Hazus 5.1. FEMA US; 2022.
- [30] Youd TL, Idriss IM, Andrus RD, Arango I, Castro G, Christian JT, et al. Liquefaction resistance of soils: summary report from the 1996 NCEER and 1998 NCEER/NSF workshops. *J Geotech Geoenviron Eng* 2001;127:297–313. [https://doi.org/10.1061/\(ASCE\)1090-0241\(2001\)127:4\(297\)](https://doi.org/10.1061/(ASCE)1090-0241(2001)127:4(297)).
- [31] Cetin KO, Seed RB, Der Kiureghian A, Tokimatsu K, Harder LF, Kayen RE, et al. Standard penetration test-based probabilistic and deterministic assessment of seismic soil liquefaction potential. *J Geotech Geoenviron Eng* 2004;130(12):1314–40. [https://doi.org/10.1061/\(ASCE\)1090-0241\(2004\)130:12\(1314\)](https://doi.org/10.1061/(ASCE)1090-0241(2004)130:12(1314)).
- [32] Boulanger RW, Idriss IM. CPT and SPT based liquefaction triggering procedures. Report No. UCD/CGM-14/01. Center for Geotechnical Modeling, University of California, Davis; 2014.
- [33] Dafalias YF, Manzari MT. Simple plasticity sand model accounting for fabric change effects. *J Eng Mech* 2004;130(6):622–34.
- [34] Boulanger RW, Ziotopoulou K. PM4Sand (Version 3.1): A sand plasticity model for earthquake engineering applications. Report No. UCD/CGM-17/01. Center for Geotechnical Modeling, Department of Civil and Environmental Engineering, University of California, Davis; 2017.
- [35] Zhang Y, Xue D, Zhou S, Zhang M, Wen H. In: Simulation analysis of the effects of liquefaction on pile foundations under seismic response. Singapore: Springer; 2024. p. 526. [https://doi.org/10.1007/978-981-97-4355-1\\_17](https://doi.org/10.1007/978-981-97-4355-1_17).
- [36] Beaty M, Byrne P. An effective stress model for predicting liquefaction behaviour of sand. *Geotech Earthq Eng Soil Dyn* III 1998;75(1):766–77.
- [37] Byrne PM. A cyclic shear-volume coupling and pore-pressure model for sand. In: Proceedings of the Second International Conference on Recent Advances in Geotechnical Earthquake Engineering and Soil Dynamics, St. Louis, MO, USA, 11–15 March 1991; 1991. p. 47–55.
- [38] Ecemis N. Experimental and numerical modeling on the liquefaction potential and ground settlement of silt-interlayered stratified sands. *Soil Dyn Earthq Eng* 2021;144(10):106691. <https://doi.org/10.1016/j.soildyn.2021.106691>.
- [39] Zalachoritis G, Zekkos D, Athanasopoulos-Zekkos A, Gerolymos N. The role of liquefaction on the seismic response of quay walls during the 2014 Cephalonia, Greece, earthquakes. *J Geotech Geoenviron Eng* 2021;147(12):04021137.
- [40] Youd TL, Perkins DM. Mapping of liquefaction-induced ground failure potential. *J Geotech Eng Div* 1978;104(4):433–46. <https://doi.org/10.1061/AJGEB.6.0000612>.
- [41] Wakamatsu K. Evaluation of liquefaction susceptibility based on detailed geomorphological classification. In: In: Proceedings of the Annual Meeting of Architectural Institute of Japan; 1992. p. 1443–4.
- [42] CDMG. Guidelines for analyzing and mitigating liquefaction hazards in California. California Department of Conservation, Division of Mines and Geology, Special Publication 117; 1999.
- [43] Witter RC, Knudsen KL, Sowers JM, Wentworth CM, Koehler RD, Randolph CE, et al. Maps of Quaternary deposits and liquefaction susceptibility in the central San Francisco Bay region. California US Geological Survey Open-File Report 2006–1037 2006. Scale 1:100,000.
- [44] Barnhart WD, Yeck WL, McNamara DE. Induced earthquake and liquefaction hazards in Oklahoma, USA: Constraints from InSAR. *Remote Sens Environ* 2018;218:1–12. <https://doi.org/10.1016/j.rse.2018.09.005>.
- [45] Albano M, Chiaradonna A, Saroli M, Moro M, Pepe A, Solaro G. InSAR analysis of post-liquefaction consolidation subsidence after 2012 Emilia earthquake sequence (Italy). *Remote Sens* 2024;16:2364. <https://doi.org/10.3390/rs16132364>.
- [46] Lakkimsetti B, Latha GM. Role of geofoam inclusions on the liquefaction resilience of transportation geostructures. *Transp Geotech* 2023;41:101041. <https://doi.org/10.1016/j.trgeo.2023.101041>.
- [47] Amanta AS, Dasaka SM. Air injection method as a liquefaction countermeasure for saturated granular soils. *Transp Geotech* 2021;30:100622. <https://doi.org/10.1016/j.trgeo.2021.100622>.
- [48] Taftosoglou M, Valkaniotis S, Papathanassiou G, Klimis N, Dokas I. A detailed liquefaction susceptibility map of Nestos River Delta, Thrace, Greece based on surficial geology and geomorphology. *Geosciences* 2022;12(10):361. <https://doi.org/10.3390/geosciences12100361>.
- [49] Iwasaki T, Tatsuoka F, Tokida K, Yasuda S. A practical method for assessing soil liquefaction potential based on case studies at various sites in Japan. In: In: Proceedings of the 2nd International Earthquake Microzonation Conference; 1978. p. 885–96.
- [50] van Ballegooij S, Malan P, Lacrosse V, Jacka M, Cubrinovski M, Bray J, et al. Assessment of liquefaction-induced land damage for residential Christchurch. *Earthq Spectra* 2014;30(1):31–55. <https://doi.org/10.1193/031813EQS0709>.
- [51] Toprak S, Holzer TL. Liquefaction potential Index: Field assessment. *J Geotech Geoenviron Eng* 2003;129(4):315–22. [https://doi.org/10.1061/\(ASCE\)1090-0241\(2003\)129:4\(315\)](https://doi.org/10.1061/(ASCE)1090-0241(2003)129:4(315)).
- [52] Idriss IM, Boulanger RW. Soil liquefaction during earthquakes. Monograph MNO-12. Earthquake Engineering Research Institute (EERI) 2008.
- [53] Moss RES, Chen G. Comparing liquefaction procedures in the U.S. and China. In: 14th World Conference on Earthquake Engineering, Beijing, China, October 12–17, 2008.
- [54] Zhu J, Daley D, Baise LG, Thompson EM, Wald DJ, Knudsen KL. A Geospatial Liquefaction Model for Rapid Response and Loss Estimation. *Earthquake Spectra* 2015; 31(3): 181–200. Springer, USA. Doi: 10.1193/121912EQS353M.
- [55] Tokimatsu K, Seed HB. Evaluation of settlements in sands due to earthquake shaking. *Journal of Geotechnical Engineering*. 1987;113(8):861–878. doi: 10.1061/(ASCE)0733-9410(1987)113:8(861).
- [56] Ishihara K, Yoshimine M. Evaluation of settlements in sand deposits following liquefaction during earthquakes. *Soils Found* 1992;32(1):173–88. <https://doi.org/10.3208/sandf1972.32.173>.
- [57] Zhang G, Robertson PK, Brachman RWI. Estimating liquefaction-induced ground settlements from CPT for level ground. *Can Geotech J* 2002;39(5):1168–80. <https://doi.org/10.1139/t02-047>.
- [58] Toyota H, Takada S. Settlement assessment of sand subjected to cyclic stress related to a load moving over a surface using hollow-cylindrical torsional shear apparatus. *Transport Geotechnics* 2021;29:100580. <https://doi.org/10.1016/j.trgeo.2021.100580>.
- [59] Chiaradonna A, Tropeano G, d'Onofrio A, Silvestri F. Development of a simplified model for pore water pressure build-up induced by cyclic loading. *Bull Earthq Eng* 2018;16(9):3627–52. <https://doi.org/10.1007/s10518-018-0354-4>.
- [60] Chiaradonna A, d'Onofrio A, Bilotta E. Assessment of post-liquefaction consolidation settlement. *Bull Earthq Eng* 2019;17. <https://doi.org/10.1007/s10518-019-00695-0>. Article 695.
- [61] Argyroudis SA. Resilience metrics for transport networks: a review and practical examples for bridges. *Proc Inst Civ Eng - Bridge Eng* 2022;175(3):179–92. <https://doi.org/10.1680/jbren.21.00075>.
- [62] McKenna G, Argyroudis SA, Winter MG, Mitoulis SA. Multiple hazard fragility analysis for granular highway embankments: Moisture ingress and scour. *Transp Geotech* 2021;26:100431. <https://doi.org/10.1016/j.trgeo.2020.100431>.
- [63] Papatheodorou K, Theodoulidis N, Klimis N, Zulfikar C, Vintila D, Cardanet V, et al. Rapid earthquake damage assessment and education to improve earthquake response efficiency and community resilience. *Sustainability* 2023;15(24):16603. <https://doi.org/10.3390/su152416603>.
- [64] Caputo R, Chatzipetros A, Pavlides S, Sboras S. The Greek Database of Seismogenic sources (GreDaSS): State-of-the-art for northern Greece. *Ann Geophys* 2012;55(5):859–94. <https://doi.org/10.4401/ag-5168>.
- [65] Giardini D, Wössner J, Danciu L. Seismic Hazard Harmonization in Europe (SHARE): Online Data. Resource 2013. <https://doi.org/10.12686/SED-00000001-SHARE>.
- [66] Stewart JP, Klimis N, Savvaidis A, Theodoulidis N, Zargli E, Athanasopoulos G, et al. Compilation of a local Vs profile database and its application for inference of Vs30 from geologic- and terrain-based proxies. *Bull Seismol Soc Am* 2014;104(6):2827–41. <https://doi.org/10.1785/0120130331>.
- [67] Chiou B-S-J, Youngs RR. Update of the Chiou and Youngs NGA Model for the Average Horizontal Component of Peak Ground Motion and Response Spectra. *Earthq Spectra* 2014;30(3):1117–53. <https://doi.org/10.1193/072813EQS219M>.
- [68] Boore D, Stewart J, Skarlatoudis A, Seyhan E, Margaris B, Theodoulidis N, et al. A ground-motion prediction model for shallow crustal earthquakes in Greece. *Bull Seismol Soc Am* 2021;111(2):857–74. <https://doi.org/10.1785/0120200270>.
- [69] Sotiriadis D, Margaris B, Klimis N, Dokas IM. Seismic Hazard in Greece: a Comparative Study for the Region of East Macedonia and Thrace. *GeoHazards* 2023;4:239–66. <https://doi.org/10.3390/geohazards4030014>.
- [70] YDROEREUNA. Hydrological Survey of Alluvial Area in Delta of Nestos. YDROEREUNA, Athens, Greece; 1978 (in Greek).
- [71] Stournaras G. Evolution et Comportement d'un Système Aquifer Hétérogène. Geologie et Hydrogeologie du Delta Nestos (Greece) et de ses Bordures. Doctoral Thesis, University Grenoble, Grenoble, France; 1984.

- [72] YDRODOMIKI. Economic Feasibility Study of Irrigation in Rhodope-Xanthi-Kavala and Drama Districts by Thisavros-Temenos Dams of Nestos River. Department of Agriculture, Athens, Greece; 1985 (in Greek).
- [73] Gkiougkis I, Pouliaris C, Pliakas FK, Diamantis I, Kallioras A. Conceptual and Mathematical Modeling of a Coastal Aquifer in Eastern Delta of R. Nestos (N Greece) *Hydrology* 2021;8(1):23. <https://doi.org/10.3390/hydrology8010023>.
- [74] Florida Department of Transportation. Airport Costs: Transportation Costs Report. Florida Department of Transportation; April 15, 2011. Costs for airport runway, taxiway, ramp, terminal, and fuel-tank construction and repair. Available from: Florida Department of Transportation, Planning & Policy Office (original report).
- [75] Trump BD, Mitoulis S, Argyroudis S, Kiker G, Palma-Oliveira J, Horton R, et al. Threat-agnostic resilience: Framing and applications. *Int J Disaster Risk Reduct* 2025;124:105535. <https://doi.org/10.1016/j.ijdrr.2025.105535>.
- [76] Lajoie KR, Helley EJ. Differentiation of sedimentary deposits for purposes of seismic zonation. *US Geol Surv Prof Pap* 1975. p. A39–A51.
- [77] Helley EJ, Lajoie KR. Flatland deposits of the San Francisco Bay region, California: their geology and engineering properties, and their importance to comprehensive planning. *US Geological Survey Professional Paper* 943 1979;88:pp.
- [78] AGS. Technical Memorandum No. 2: Geotechnical Study for Runway Safety Areas, Oakland International Airport; 2008.
- [79] Vallerga BA, Grogan WP. A case study: damage to the Metropolitan Oakland International Airport caused by the Loma Prieta Earthquake. Washington, DC: Final Report; 1992.
- [80] William Lettis & Associates, Inc. Evaluation of earthquake-induced liquefaction hazards at San Francisco Bay Area commercial airports. Report prepared for the Association of Bay Area Governments; 1999. 37 p.
- [81] Plafker G, Galloway JP. Lessons learned from the Loma Prieta, California, Earthquake of October 17, 1989. USGS Circular 1045; 1989. Doi: 10.3133/circ1045.
- [82] Beetham D, Beattie G, Earl B, Duncan D. NZ society for earthquake engineering reconnaissance team to Seattle, USA: the February 28, 2001 Nisqually earthquake. *Bull N Z Soc Earthq Eng* 2001;34(4):253–75. <https://doi.org/10.5459/bnzsee.34.4.253-275>.
- [83] Nisqually Earthquake Clearinghouse Group. The Nisqually Earthquake of 28 February 2001: Preliminary Reconnaissance Report. University of Washington, Seattle, WA; 2001.
- [84] Washington Division of Geology and Earth Resources. Surface geology, 1: 100,000—GIS data, November 2016. Digital Data Series DS-18, version 3.1. Washington Division of Geology and Earth Resources; 2016. Previously released June 2010.
- [85] Kılıç S, Evrendilek F, Berberoglu S, Demirkesen A. Environmental monitoring of land-use and land-cover changes in a Mediterranean region of Turkey. *Environmental Monitoring and Assessment* 2006;114:157–68. <https://doi.org/10.1007/s10661-006-2525-z>.
- [86] Bol E, Özocak A, Sert S, Çetin KÖ, Arslan E, Kocaman K, et al. Evaluation of soil liquefaction in the city of Hatay triggered after the February 6, 2023 Kahramanmaraş-Türkiye earthquake sequence. *Eng Geol* 2024;339:107648. <https://doi.org/10.1016/j.enggeo.2024.107648>.
- [87] Bol E. The geotechnical properties of Adapazari soils (in Turkish). *Adapazari: Sakarya University*; 2003. Graduate thesis.
- [88] Juang CH, Ching J, Wang L, Khoshnevisan S, Ku CS. Simplified procedure for estimation of liquefaction-induced settlement and site-specific probabilistic settlement exceedance curve using cone penetration test (CPT). *Can Geotech J* 2013;50(10):1055–66. <https://doi.org/10.1139/cgj-2012-0410>.
- [89] Yanites BJ, Clark MK, Roering JJ, West AJ, Zekkos D, Baldwin JW, et al. Cascading land surface hazards as a nexus in the Earth system. *Science* 2025;388(6754). <https://doi.org/10.1126/science.adp9559>.
- [90] Horton R, Trump BD, Trump J, Knowles HS, Linkov I, Jones P, et al. Performance metrics for resilience of airport infrastructure. *Transp Res Part D-Transp Environ* 2025;142:104676. <https://doi.org/10.1016/j.trd.2025.104676>.